NTNU – Trondheim
Norwegian University of
Science and Technology

The Susceptibility to Hydrogen Induced Stress Cracking for Alloy 718 and Alloy 725

Gaute Stenerud

Materials Science and Engineering
Submission date: June 2014
Supervisor: Roy Johnsen, IPM
Co-supervisor: Afrooz Barnoush, IPM

Norwegian University of Science and Technology
Department of Engineering Design and Materials

Abstract

The Hydrogen Induced Stress Cracking (HISC) susceptibility of Alloy 718 and Alloy 725 were examined and compared. Pre-charged samples of each alloy were stepwise loaded during cathodic polarization in Cortest Proof rings. After fracture the fracture surfaces were examined in scanning electron microscope and the hydrogen concentration was measured by SINTEF – Materials and Chemistry. To find a safe load level were HISC did not occur, pre-charged samples of each alloy were loaded to a percentage of the fracture load for 30 days during cathodic polarization.

It was found that both alloys are severely embrittled by hydrogen. Both the ductility and the stress at fracture were reduced for both alloys. There was no clear difference in how much the ductility and strength were reduced for the two alloys. The constant load tests revealed a safe stress at 123,8 % of yield strength (YS) for Alloy 725 and 120,4 % of YS for Alloy 718. Based on this it was concluded that Alloy 725 is more resistant to HISC than Alloy 718.

Sammendrag

Motstanden mot hydrogenindusert sprekking (HISC) for *Alloy 718* og *Alloy 725* ble undersøkt og sammenlignet. Forladede prøver av hver legering ble stegvis lastet i *Cortest Proof* ringer under katodisk polarisering. Etter brudd ble bruddflatene undersøkt i elektronmikroskop og hydrogenkonsentrasjonen ble målt av SINTEF – Materialer og Kjemi. Resultatene fra denne testingen ble brukt til å finne et trygt lastnivå hvor HISC ikke ville skje. For å bekrefte at dette var et trygt lastnivået ble forladede prøver lastet til en prosent av dette nivået og holdt der i 30 dager.

Det ble konkludert med at begge legeringene er mottagelig for HISC. Både duktiliteten og spenning ved brudd ble for hver legering. Det var ingen klar forskjell i reduksjon av styrke og duktilitet mellom de to legeringene. 123,8 % og 120,4% av flytespenningen ble funnet til å være trygg last for henholdsvis Alloy 725 og Alloy 718. Basert på dette ble det konkludert med at Alloy 725 er mer motstandsdyktig mot HISC enn Alloy 718.

Preface

This master thesis is submitted to NTNU as a part of the Master's degree program at the department for Material Science and Engineering. Professor Roy Johnsen has supervised this work with Professor Afrooz Barnoush and Ph.D Jim Stian Olsen as co-supervisors.

I would like to thank my supervisors for sharing their knowledge and helping me finish this master thesis. Frequent meetings and discussions improved the quality of this work. I would also like to extend my gratitude to my fellow students Ola M. Krosness and Adrian Haaland for our productive cooperation in the lab.

Finally I would like to thank Yingda Yu for sharing his experience with SEM, Nils-Inge J. Nilsen for help solving practical problems in the lab and Ann-Karin Kvernbråten for preforming the hydrogen analysis.

Trondheim, 12. June 2014.

Gaute Stenerud

Table of content

List of Abbreviations

Ag/AgCl	Silver/Silver Chloride reference electrode
AIDE	Adsorption-induced dislocation emission
Al	Aluminium
ASTM	American Society for Testing and Materials
B	Boron
BCC	Body Centred Cubic
Bi	Bismuth
C	Carbon
Ca	Calcium
CF	Corrosion Fatigue
Co	Cobalt
Cr	Chromium
Cu	Cobber
DDS	Duplex Stainless Steel
FCC	Face Centred Cubic
Fe	Iron
H	Hydrogen
H_3PO_4	Phosphoric Acid
HE	Hydrogen embrittlement
HEAC	Hydrogen-Environment-Assisted Cracking
HEDE	Hydrogen Enhanced Decohesion
HELP	Hydrogen Enhanced Local Plasticity
$Hg/HgSO_4$	Mercury/Mercurous Sulphate Electrode
HIP	Hot Isostatically Pressed
HISC	Hydrogen Induced Stress Cracking
Hr	Hour
HRC	Rockwell Hardness Scale "C"
IHAC	Internal Hydrogen Assisted cracking
ISO	International Organization for Standardization
LME	Liquid Metal Embrittlement
LVFESEM	Low Voltage Field Emission Scanning Electron Microscope

MC	Metal-Carbide
Mg	Magnesium
Mn	Manganese
Mo	Molybdenum
NACE	National Association of Corrosion Engineers
NaCl	Sodium Chloride
Nb	Niobium
NHE	Normal Hydrogen Electrode
Ni	Nickel
P	Phosphorous
Pb	Lead
Pd	Palladium
RA	Reduction of area
RRA	Reduction in reduction of area
S	Sulphur
SCC	Stress Corrosion Cracking
SCE	Standard Calomel Electrode
SDSS	Super Duplex Stainless Steel
Se	Selenium
SEM	Scanning Electron Microscope
Si	Silicon
Sn	Tin
SSC	Sulphide Stress Cracking
SSRT	Slow Strain Rate Testing
STD dev	Standard Deviation
Ta	Tantalum
Ti	Titanium
UNS	Unified Numbering System
UTS	Ultimate Tensile stress
wppm	Weight parts per million
YS	Yield stress

1. Introduction

1.1. Background

Nickel alloys are often used subsea in critical components exposed to both seawater and well fluid. Their acceptable corrosion resistance and high strength makes them suitable for these applications. These high strength nickel alloys can however suffer from Hydrogen induced stress cracking (HISC). Max hardness levels of the different alloys are applied to avoid this problem [1]. This is very effective to reduce the embrittlement in sour service environment, but it does not predict well how the material will respond to several years of hydrogen absorption and diffusion.

Alloy 718 (UNS N07718) and Alloy 725 (UNS N07725) are two examples of such nickel alloys. They are both precipitation-hardened alloys that can be used subsea. Alloy 718 is sour service certified for hardness values up to 40 HRC (35HRC if hot worked)[2]. This value gives the optimum combination of strength, ductility, toughness and cracking resistance. Alloy 718 is not corrosion resistant in seawater and must therefore be connected to a cathodic protection system. Alloy 725 is sour service certified for hardness values up to 43 HRC[2]. Due to its higher alloying content, it is considered immune to corrosion in seawater and can be used without cathodic protection. It may, on the other hand, be connected to other materials in need of such protection systems. Such a protection system will generate hydrogen on the protected component, which again can cause HISC in certain alloys. If a susceptible material is applied a tensile load, while in a hydrogen containing environment it may fail due to HISC. Previously, it was assumed that Alloy 718 and Alloy 725 is immune to HISC. Due to unexpected failures, this assumption has been questioned[3-5].

1.2. Aim of this work

This project will try to measure HISC susceptibility of Alloy 718 and Alloy 725 by an accelerated pre-charging process and stepwise loading tests. The main objective is to determine if the alloys are susceptible to HISC. If they are, a maximum load at which HISC does not occur will be found. In addition, the hydrogen concentration will be measured at the end of the tests.

2. Theory

Three different parameters are required for hydrogen induced stress cracking (HISC) to occur. These three are a hydrogen source, an external or internal stress and a susceptible material (presented in Figure 1). This chapter will focus on the three mentioned parameters, the mechanics behind HISC and finish of with a summary from the existing literature on this subject. First, some basic properties will be defined.

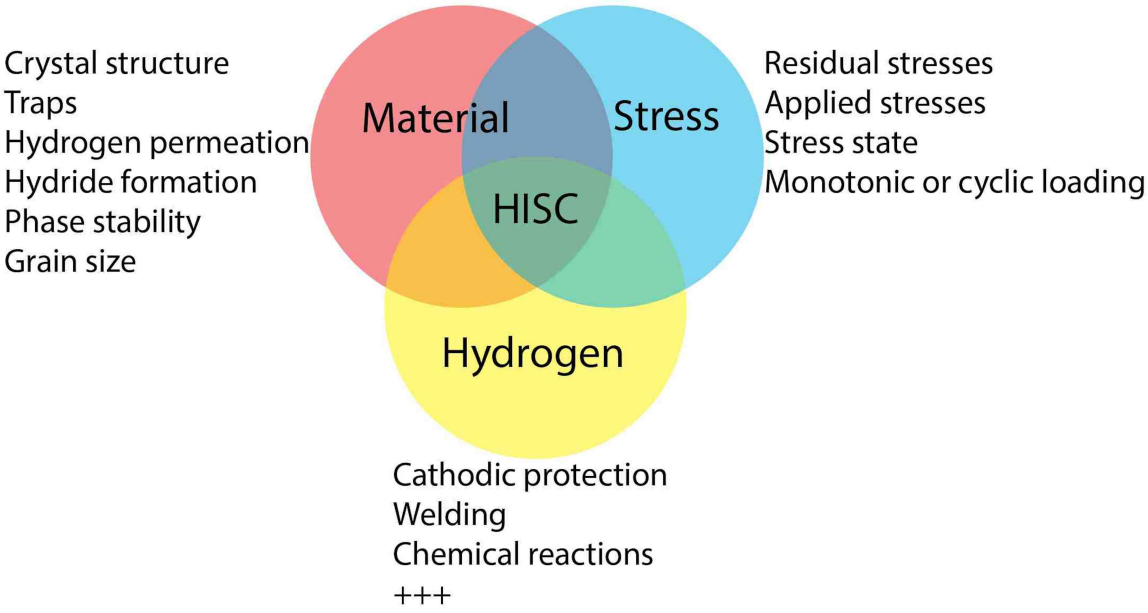

Figure 1: The factors needed for HISC to occur, and examples of such factors. This figure is inspired by figure 2.0.1 in K. Andersons work [6].

2.1. Material testing and characterization

2.1.1. Tensile testing

A tensile test is often preformed to be able to understand how a material responds to an applied force. A sample with standard dimensions is subjected to uniaxial tension while the force and strain is recorded. The strain is recorded by an extensometer. The force is usually converted to stress and plotted against the strain. From this graph, the ultimate tensile strength (UTS), yield strength (YS), fracture stress and their corresponding strains can be found, as shown in Figure 2.

The stress can be calculated with respect to the nominal area, or continuously calculated with the measured area. The two different graphs achieved are called engineering

stress-strain curve and true stress-strain curve, respectively. Figure 2 is an example of an engineering stress-strain curve.

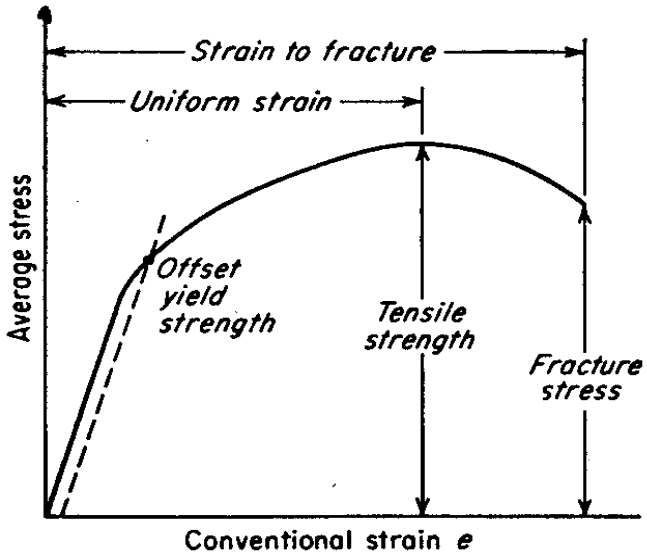

Figure 2: A sketch of a typical stress-strain curve. This figure is a copy of figure 8.1 in Dieter [7].

The YS and the UTS are two very important properties for a material. The YS tells us when yielding (plastic deformation) occurs. It is usually determined by finding the offset yield strength, the stress required to produce a specified deformation. The Offset yield strength is determined by the intersection of the stress-strain curve and a line parallel to the elastic part of the curve at an offset by a specified strain (usually 0,2%)[7]. Up to this point, the stress is related to the strain by Hooke's law.

$$\sigma = E\varepsilon \tag{1.}$$

Where σ is the applied stress, E is the young's modulus and ε is the strain. After the yield point is reached, plastic deformation occurs and this relationship is no longer valid. Most materials will strain harden at this point and the stress will continue to increase with the strain until the UTS is reached. Due to conservation of volume, the cross sectional area will be reduced when the tensile bar is strained (see Figure 3), causing a higher true stress. This reduction of area is outweighed by the strain hardening until UTS is reached. Here, the strain hardening is outweighed by the reduction of area and necking

occurs. Since the stress is calculated with respect to the nominal area and not the true area, the stress decreases with strain after this point.

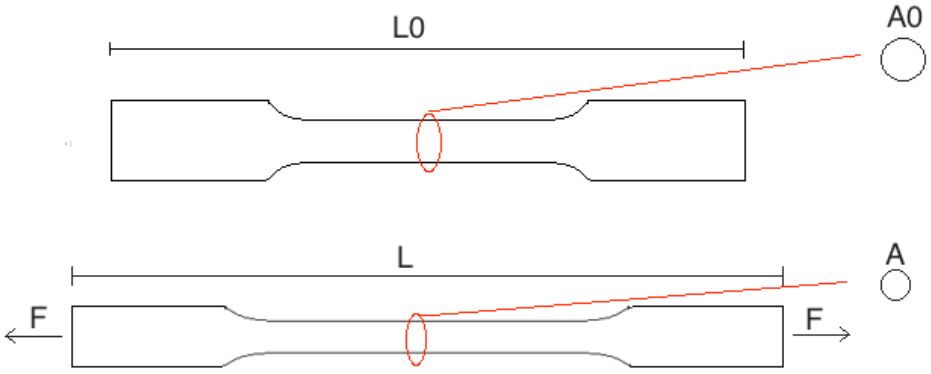

Figure 3: This figure illustrates how the cross sectional area is affected by a strain in the length direction. When tensile bar is loaded, it will be strained from *L0* to *L*. The cross sectional area is the reduced from *A0* to *A* by the consistency of volume relationship.

Ductility is another important material property and indicates how much a material can be deformed without fracture. The ductility can be found by a conventional tensile test and is quantified as elongation at break or reduction of cross sectional area (RA). When necking occurs, most of the plastic deformation is concentrated to a local region. The elongation value obtained from the test will therefore depend on the gage length over which the measurement was obtained. This does not affect the RA measurements, which is therefore a more accurate value for the ductility[7]. The RA can be found by measuring the diameter of the specimen before and after fracture. The following equation can then be used:

$$RA = \frac{A_0 - A}{A_0} \times 100 = \frac{r_0^2 - r^2}{r_0^2} \times 100 \qquad (2.)$$

Where A_0 and A is the area before and after fracture respectively, while r_0 and r is the radius before and after fracture respectively.

2.1.2. Load in a Cortest proof ring

In this project, Cortest proof rings are used for the HISC testing. A simple sketch of such a ring is included in Figure 4. Here, a tensile bar is mounted in a stainless steel ring. It is attached to a static screw in the bottom of the ring and a fastening screw on the top of

the ring. The top screw can be fastened to increase the deflection in the ring. The specimen is the then compressing the ring, which in return is exercising a tensile load on the specimen. This load is controlled by the deflection in the ring where the two are related by the following equation:

$$\Delta D = \frac{F - b}{a} \tag{3.}$$

Where F is the desired load, ΔD is the corresponding deflection, while a and b are constants for the ring. If the ring diameter at no load is known, one can simply subtract this deflection and find the next diameter. The constants are determined and supplied by the producer of the rings. These constants are used to produce a conversion chart, which calculates the deflection needed to obtain a certain load.

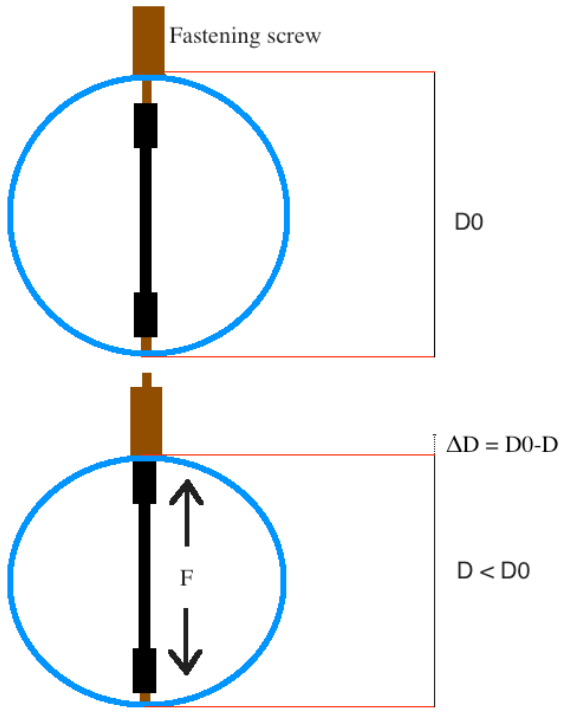

Figure 4: A simple sketch of a Cortest proof ring. In the first ring, no load is applied and the ring is at its original diameter, D0. In the ring below, the fastening screw has been used to reduce the ring diameter to D. The tensile bar is now maintaining the ring deflection by exercising a compressive force on the ring. In return, the ring is exercising a tensile load on the specimen.

2.1.3. Grain size

Another important parameter for a material is the grain size. Within one grain, the atoms are arranged identically. The interphase between two grains is called grain boundary area. This interphase is usually a few nanometre wide and can be treated as irregularities in the material. The grain boundaries disrupt the motion of dislocations and therefore increase the strength of the materials. The relationship between strength and grain size is described by the Hall-Petch relationship:

$$\sigma_y = \sigma_0 + \frac{k}{\sqrt{d}} \tag{4.}$$

Where σ_y is yield strength, σ_0 and k are constants and d is the grain size[8].
Small grains are often desired due to its positive effect on strength, toughness and ductile to brittle transition temperature[7].

2.2. Fracture mechanics in metals

Fracture mechanics differ between ductile and brittle fracture. Ductile materials usually fail due to void nucleation, growth and coalescence. The voids nucleate at second phase particles, inclusions and carbides. Once these voids are formed, they will grow due to further plastic strain and hydrostatic stress (Figure 5 (a)). When the voids coalescence, a penny-shaped flaw is formed in centre of the specimen (Figure 5 (b)). The flaw grows perpendicular to the direction of the applied stress until it reaches the surface. Here, deformation bands are often formed 45° to the stress direction. This concentrates the strain to a small area, causing voids to form at smaller particles (Figure 5 (d)). A high concentration of voids along the 45° axis is formed, and total fracture occurs. This gives the characteristic cup and cone fracture surface (Figure 5 (c)). Another way of recognizing ductile fracture is the dimples formed on the fracture surface (see Figure 6). Inclusion or secondary particles can often be observed in the bottom of these dimples[7, 9].

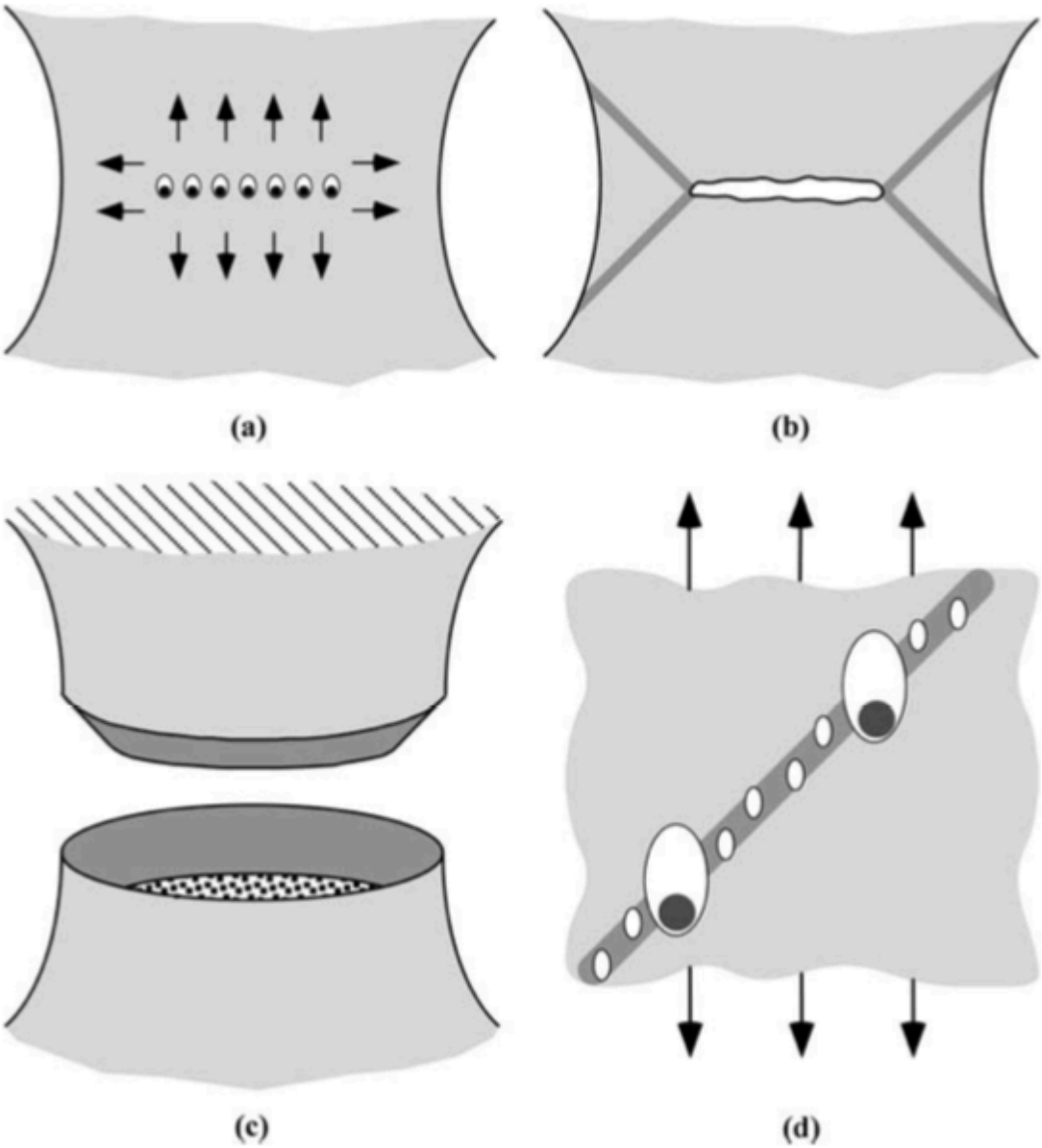

Figure 5: An illustration of how the cup and cone fracture occurs during uniaxial tension. (a) Shows growth of already nucleated voids, (b) shows the formation of a penny shaped flaw and deformation bands, (d) shows nucleation of voids at smaller particles along the deformation band while (c) shows the cup and cone fracture. This illustration is a copy of figure 5.6 in "Fracture mechanics: Fundamentals and Applications" by T.L Anderson [9].

Brittle fracture in metals occurs by two different mechanisms, either cleavage or intergranular fracture. Although cleavage is a brittle fracture mechanism, it may be preceded by ductile crack growth. First a crack has to be nucleated. This can be done by plastic deformation, which involves dislocation pile up at grain boundaries. This pile up of dislocations can form a microcrack. Another way of forming a microcrack can be cracking of inclusions, carbides or secondary phase particles. When a crack is produced,

it propagates along a particular crystallographic plane[9]. The crack propagates through the grains along the planes with the lowest packing density. Therefore the cleavage crack changes direction every time it crosses a grain boundary. If the fracture surface is examined, cleavage fracture can be recognised by its characteristic river pattern through the grain [7]. Figure 7 shows a scanning electron microscope (SEM) picture of a typical cleavage fracture surface.

Under special circumstances, such as environmentally assisted cracking, metals can fail along the grain boundaries. This is called intergranular fracture. Intergranular fracture occurs when the grain boundaries is the easiest way for crack propagation. This is not a very common fracture mechanism, but may be present in materials exposed to certain environments or improper tempering. This type of fracture can be recognised by a faceted fracture surface[7, 9], as shown in Figure 8.

As mentioned, the environment can affect the fracture mechanics of metals. Examples of this are[9]:

- **Stress corrosion cracking (SCC)**, where susceptible materials can suffer premature fracture when a tensile stress is applied in a corrosive environment.
- **Hydrogen embrittlement (HE)** can occur when susceptible materials are used in a hydrogen-containing environment. The material will undergo a drastic loss in ductility.
- **Sulphide stress cracking (SSC)** is a form of hydrogen embrittlement where H_2S reacts with the material surface, creating atomic hydrogen. Since sulphur is a poison for hydrogen recombination, more hydrogen is introduced to the material. If the material is susceptible, it will then suffer from SSC.
- **Corrosion fatigue (CF)** is a phenomenon where the fatigue crack growth rate is enhanced by a corrosive environment.
- **Liquid metal embrittlement (LME)** can occur if a susceptible material is tested in certain liquid metals. The susceptible materials will undergo a drastic loss in ductility.

In this project the focus will be on hydrogen induced stress cracking (HISC), which may be a consequence of hydrogen embrittlement.

2.2.1. Fractography

Due to its good depth of view and high resolution, scanning electron microscopy (SEM) is often used for fractographic studies. These types of studies, examines the topography of the fracture surface. The fracture surface indicates which type of fracture mechanism has occurred. As mentioned, for transgranular cleavage fracture the crack propagates along certain crystallographic planes. This kind of fracture can be recognized by river patterns (Figure 7). Intergranular fracture can be recognized by its faceted fracture surface, as shown in Figure 8. The Faceted surface occurs because cracks propagate along grain boundaries. Figure 6 shows a dimpled fracture surface, characteristic for ductile fractures.

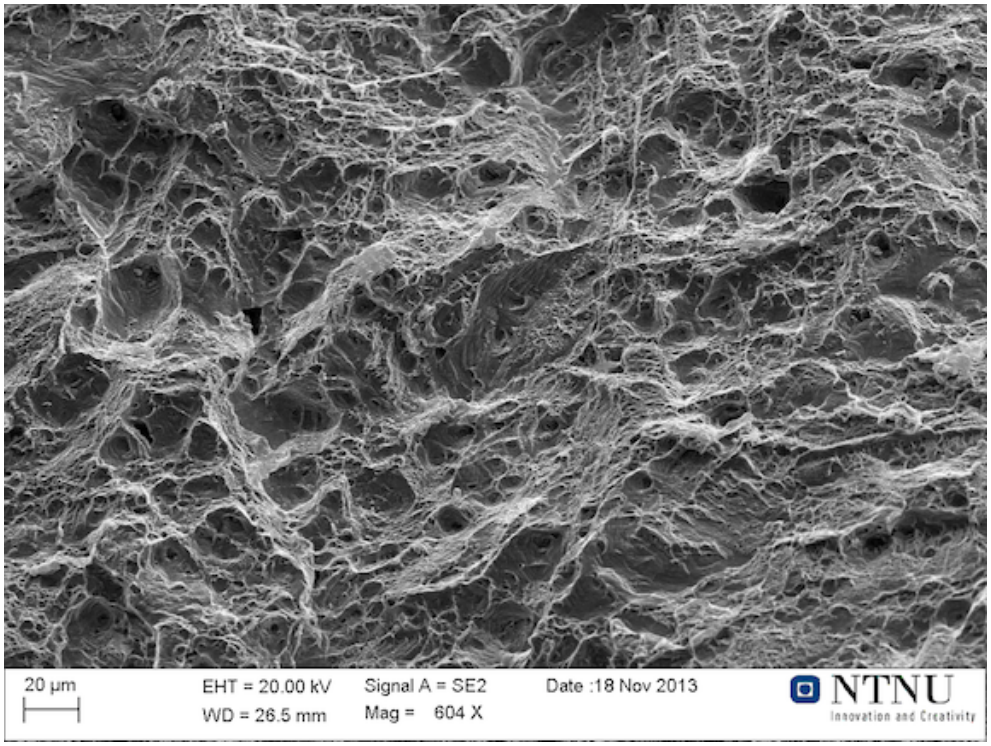

Figure 6: SEM image of ductile fracture in Alloy 718 characterized by dimples.

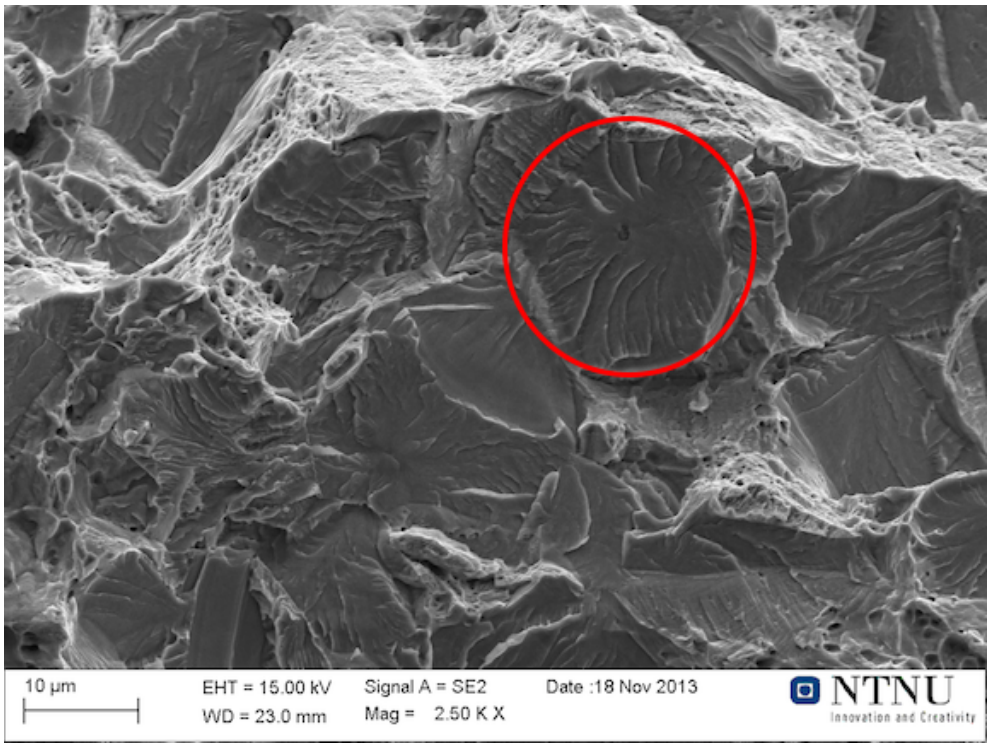

Figure 7: Shows a transgranular fracture in SDSS. The red ring shows river patterns, characteristic for transgranular fracture.

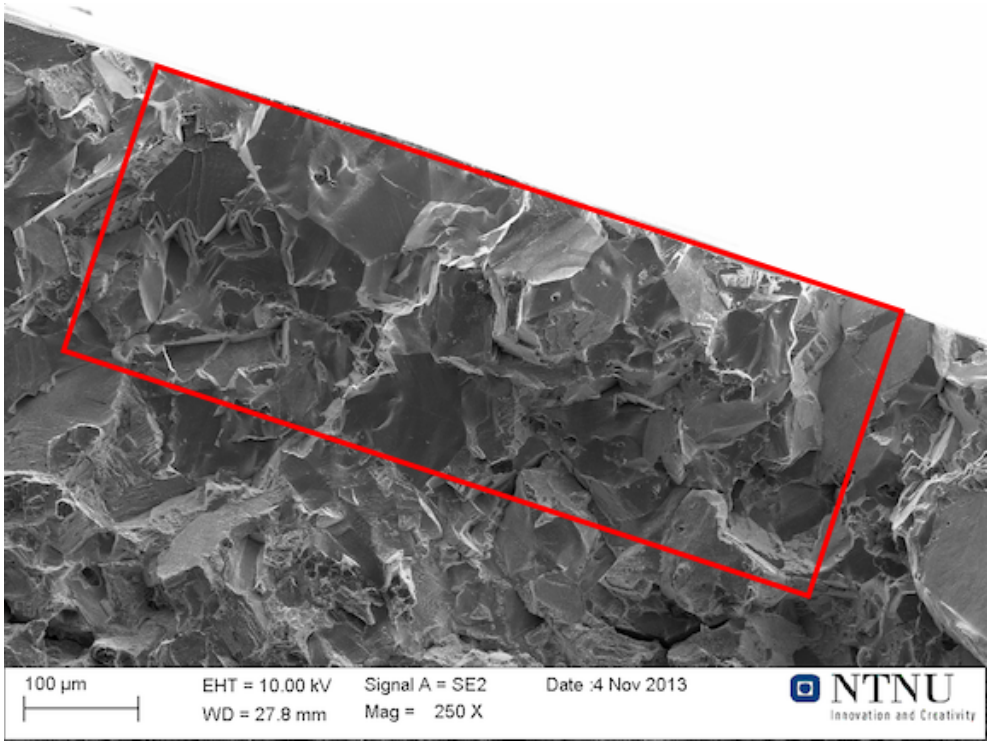

Figure 8: Shows intergranular fracture in Alloy 718. The red rectangle marks a zone where intergranular fracture dominates.

2.3. Hydrogen ingress

As mentioned, hydrogen must be present for HISC to occur. Hydrogen can be introduced to the material in several ways. Moist electrodes or material during welding, pickling, corrosion processes, cathodic protection, hydrogen containing environment among others, may introduce hydrogen to the material. The literature differs between internal-hydrogen assisted cracking (IHAC) and hydrogen-environment-assisted cracking (HEAC) [10]. The two are distinguished by how the hydrogen is introduced to the material. In IHAC the hydrogen is introduced to the material prior to use (manufacturing, processing, pickling, welding, etc.), while in HEAC the hydrogen comes from the environment where the material is used. It is believed that the hydrogen embrittlement mechanism is the same for both IHAC and HEAC. However, the location of the damage processes and incubation time for fracture will vary due to differences in kinetics of mass transport for internal and environmental hydrogen[11]. The mechanism for hydrogen embrittlement is discussed in chapter 2.4.

When Alloy 718 and Alloy 725 are used subsea, they are connected to a cathodic protection system. To be able to understand how cathodic protection (CP) affects hydrogen evolution, the electrochemistry behind corrosion must be considered. A corrosion reaction can always be divided into two or more half-cell reactions where charge transfer occurs. Oxidation reactions release electrons while reduction reactions consume electrons. Equations 5-7 show the half-cell reactions and the overall reaction for a metal M in an acidic environment where hydrogen reduction dominates. Which reduction reaction occurs will depend on the chemistry of the electrolyte. If for instance oxygen is present, oxygen reduction is possible.

Oxidation $$M \rightarrow M^{n+} + ne^{-} \quad (5.)$$

Reduction $$nH^{+} + ne^{-} \rightarrow \frac{n}{2} H_2(g) \quad (6.)$$

Overall $$M + nH^{+} \rightarrow \frac{n}{2} H_2(g) + M^{n+} \quad (7.)$$

Since these half-cell reactions are electrochemical reactions, they will be possible over a range of potentials. This range will depend on the temperature and activity of the different species.

A Pourbaix diagram connects the potential, pH and the activity of the metal considered. This diagram is very useful for evaluating if corrosion is possible for a given metal in a solution with a given pH. An example of such a Pourbaix diagram for a hypothetical metal is given in Figure 9. In the active area corrosion will occur while corrosion is not thermodynamically possible in the immune area. The metal is partially protected by an oxide layer in the passive area; this area will not be further discussed here.

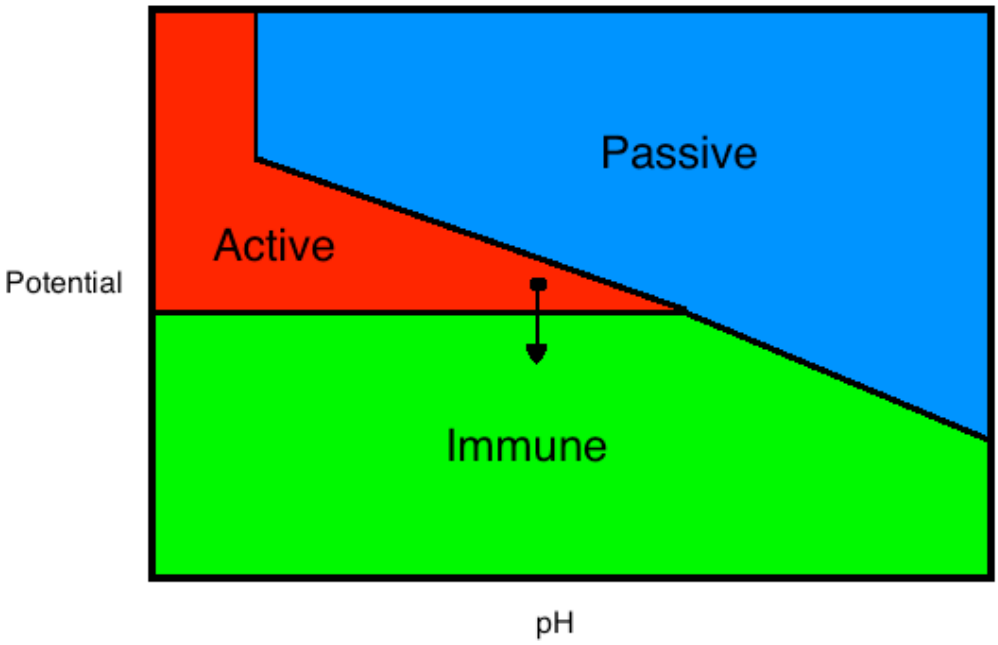

Figure 9: A Pourbaix diagram for a hypothetical metal.

The idea behind CP is to reduce the potential towards the immune area, as shown by the arrow in Figure 9. This can be done by supplying an external current to the metal. This is illustrated in the Evans diagram shown in Figure 10. This diagram presents the potential range for where the half-cell reaction is possible and at which rate they will occur. The corrosion rate (I_{Corr}) and potential (E_{Corr}) can be found from the intersection between the reduction and oxidation curves. If an external current (I_{ext}) is supplied to the metal, the potential of the metal will be reduced to the protection potential (E_{Prot}). As shown in Figure 10 the rate for metal oxidation is severely reduced and the metal is now cathodically protected. At this lower potential the reduction rate is increased, as seen in Figure 10. In addition, the hydrogen reduction dominates more than the oxygen reduction. In this way the hydrogen formation on the metal surface is increased and CP will act as a continuous supply of hydrogen.

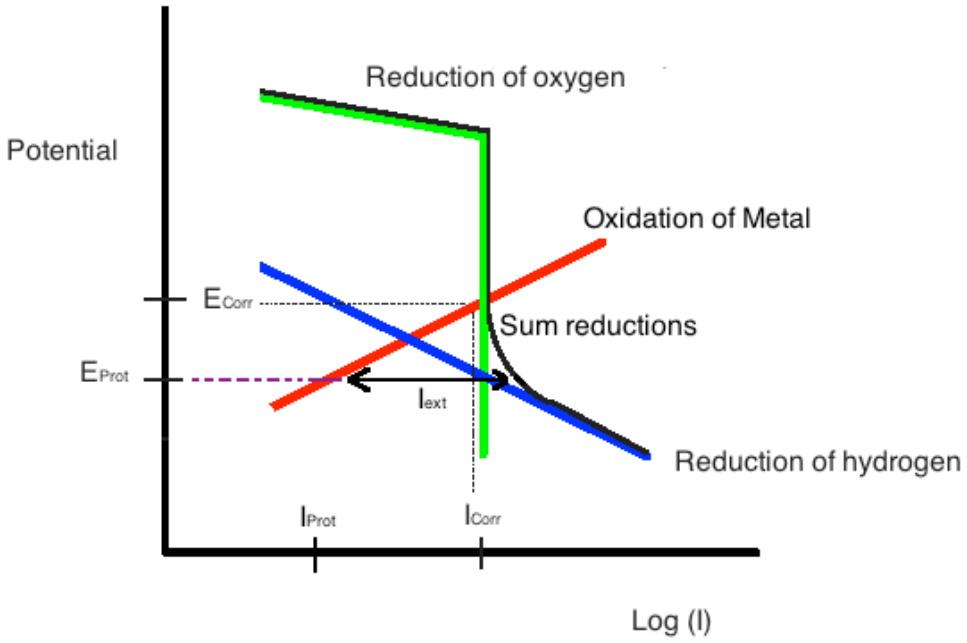

Figure 10: An Evans diagram for a hypothetical metal.

When hydrogen is reduced at the surface of a component it can either recombine to form hydrogen gas or be absorbed by the material. There are two mechanisms proposed for the hydrogen passage through the metallic interface. The classical mechanism suggests that atomic hydrogen will passage directly through the interface (8), while Crolet et al. suggests the passage of hydrogen in ionic form (9).

$$H_{ads} \rightarrow H_{abs} \quad (8.)$$

$$H^{+}_{ads} \rightarrow H^{+}_{abs} \quad (9.)$$

Independently of the mechanism, the result is the same, a subsurface concentration of hydrogen. This subsurface concentration will depend on the charging current and the kinetics of hydrogen evolution[12].

The subsurface concentration of hydrogen will give a concentration gradient, which again will give a driving force for hydrogen diffusion. Hydrogen is a small atom and can occupy interstitial sites inside the metal. In face centred cubic (FCC) structures there are one octahedral and three tetragonal sites per metal atom which hydrogen can occupy [12]. The interstitial sites in FCC structures are larger than the sites in body centred cubic (BCC) structures. This gives a higher solubility of hydrogen in FCC [13]. The

number of interstitial sites are however greater in BCC, this gives a higher diffusion rate in BCC structures.

For an ideal material with no traps, diffusion can be described by Fick's first law:

$$J = -D\frac{\mathrm{d}c}{\mathrm{d}x} \tag{10.}$$

Where J is the flux, D is the diffusion coefficient and $\mathrm{d}c/\mathrm{d}x$ is the concentration gradient [8]. The diffusion coefficient is exponentially related to the temperature. This can be seen by equation (11.):

$$D = D_0 \exp\left(\frac{-Q}{RT}\right) \tag{11.}$$

Where Q is the activation energy, R is the gas constant, T is the temperature and D_0 is the pre-exponential term. The diffusion will also obey Fick's second law, which describes the dynamic diffusion of atoms[8]. Assuming that D is not a function of location x, a simplified version of Fick's second law is obtained:

$$\frac{\partial c}{\partial x} = D\left(\frac{\partial^2 c}{\partial x^2}\right) \tag{12.}$$

The diffusion of hydrogen is also affected by stress. The stress can be either an applied stress or residual stress. Hydrogen will diffuse towards places of high stress. Even if the hydrogen is uniformly distributed (no concentration gradient) throughout the matrix, stress can induce diffusion of hydrogen [12]. This is important in most theories for hydrogen embrittlement mechanisms. If a cracked sample is loaded in tension, the stress will become concentrated around the crack. This stress concentration will enhance hydrogen diffusion to the crack tip and increase the hydrogen concentration near the crack. This is further discussed in the next chapter.

If hydrogen were only occupying interstitial sites, it would start to diffuse out of the material when the cathodic charging is halted. Most materials will however contain

traps. Any metallurgical defect in a material can act as a trap [12]. These traps are an alternative position for hydrogen atoms. Depending on the energy of the trap, it can be either reversible or irreversible [14]. Irreversible traps have a high binding energy that prevents the atoms from diffusing, while reversible traps has a binding energy level comparable to the energy of the interstitial sites. These traps lower the real diffusion rate. A good diffusion model should therefore account for this effect. Another aspect of traps is that they will keep the hydrogen inside the material and may behave as hydrogen sources or crack initiation points during deformation.

Dislocations are one of the defects that may act as a reversible trap. During plastic deformation, more dislocations are created, increasing the amount of traps. Plastic deformation also induces dislocation motion. When dislocations start to move, two things may happen. Either hydrogen will move together with the dislocation or the speed of the dislocation will be high enough to release the hydrogen from the trap. In this way dislocations can transport hydrogen to highly stressed zones, increasing the diffusion of hydrogen[12, 13].

It is proposed that grain boundary diffusion will have a high effect on the hydrogen embrittlement of metals with low lattice diffusion rate [15] [16]. Harris [17] proposed that diffusion along grain boundary for Ni may vary between 40 and 1000 time bulk diffusion. Others have reported that dislocations and vacancies along the grain boundary will reduce the diffusivity along grain boundaries [18]. The effect of grain boundaries on hydrogen diffusion is clearly controversial.

2.4. Hydrogen embrittlement

Once hydrogen has entered the material, it can be damaging in several ways. The degradation process will depend on the temperature, stress state, material, environment and hydrogen fugacity. The literature mentions high temperature hydrogen attack, hydrogen blistering and hydride formation. The most common and devastating effect is hydrogen embrittlement, which again can lead to hydrogen-induced stress cracking (HISC).

Hydrogen embrittlement may occur when atomic hydrogen is introduced into a material. If the material is susceptible to hydrogen embrittlement, the toughness and ductility is reduced dramatically. A common misperception is that only BCC metals are susceptible to hydrogen embrittlement. Extensive work on this subject has however revealed that most metals are prone to hydrogen embrittlement[9]. As mentioned, a combination of a susceptible material, an internal or external stress and a hydrogen source, can give hydrogen induced stress cracking (HISC).

The mechanism for hydrogen embrittlement remains a topic of discussion. Several viable mechanisms have been proposed and argued for. The most elaborated and well established models are the decohesion model and the hydrogen enhanced localised plasticity (HELP) model [10, 12]. In addition a hydride forming mechanism and adsorption-induced dislocation emission is discussed in the literature[19-21].

The hydride forming mechanism involves hydrogen diffusion to crack tips under the influence of a stress gradient, nucleation of a hydride phase, brittle cleavage of this hydride phase and crack arrest at the hydride/matrix interphase [19]. This mechanism is possible in hydride forming materials such as titanium, niobium, zirconium and vanadium[20]. A number of alloying systems, such as Ni, Pd, Ta and possibly stainless steels, may form “pseudo-hydrides”[21]. In other words, hydrides may form during high hydrogen fugacity conditions. According to S. P. Lynch, nickel hydrides forms only at hydrogen pressures greater than 1 GPa or excessive charging[22].

The hydrogen enhance decohesion (HEDE) model explains that hydrogen accumulates at the high stress regions near the crack tip (fracture process zone) and reduces the cohesive bonding strength between the metal atoms, thereby favouring crack propagation over slip transmission[9, 10] (this is illustrated in Figure 11). The hydrogen damage sites will be localized at a small distance from the crack tip, due to the highly localized stresses in this region. This mechanism will give an intergranuler or transgranular brittle fracture, and limited plasticity around the crack tip. It also predicts a decreased extent of the plastic zone [23]. R. A. Oriani et al. was able to support this theory by examining crack propagation and arrest by changing the hydrogen fugacity. Their work gave results that could only be explained by the decohesion theory [24].

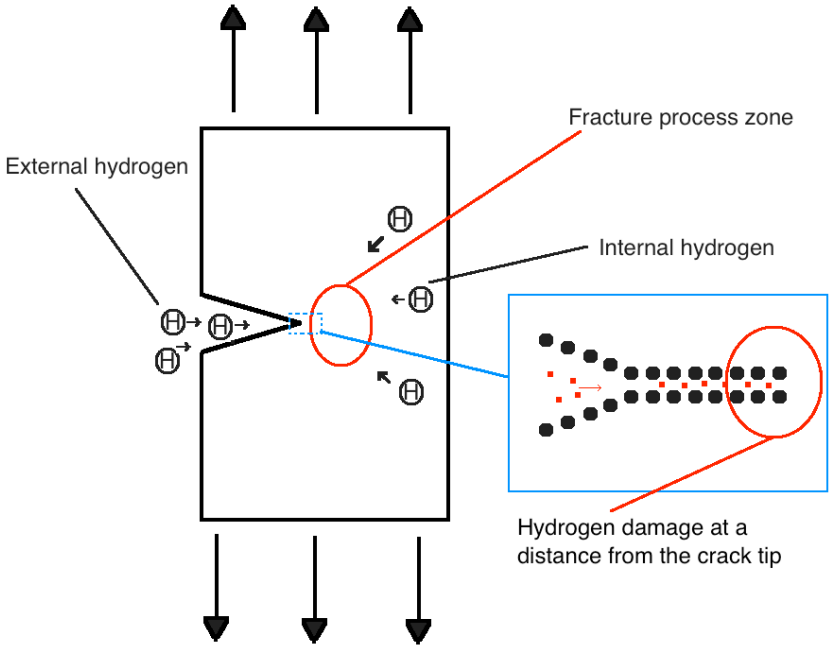

Figure 11: An illustration of how the hydrogen diffuses to a high stress region, and where the HEDE theory predicts the hydrogen damage to occur.

Another branch is based on observation of how the hydrogen affects dislocation motion. In some circumstances, hydrogen has lead to serrated yielding and hardening, while in other cases softening has been observed [12, 22]. In other words, it has been proposed that hydrogen may both inhibit and promote dislocation motion. Increased dislocation motion due to hydrogen has been directly observed using high voltage electron microscopy [22, 23]. Here, thin films of different materials are held on a certain stress level where dislocations do not move. When hydrogen is introduced, dislocation motion is observed and confirms that hydrogen eases dislocation movement. Of the plasticity models, the hydrogen enhanced localized plasticity (HELP) model is the one achieving most acknowledgement [25]. This model proposes that hydrogen accumulates near the crack tip due to the increased stresses and the triaxiality of the stress field, thereby enhancing the dislocation motion and reducing the flow stress near the crack tip. The shielding effect of hydrogen will also increase the dislocation density at the crack tip. The hydrogen reduces the interaction between dislocations and other obstacles, leading the dislocations to move closer to each other [12]. This gives a highly localized region with severe plastic deformation, enough to enable subcritical crack growth. It is proposed that due to this highly localized region, the fracture surface will be

macroscopically brittle. A closer examination should, however, indicate sever plastic deformation[20].

Lynch proposed an alternative model called adsorption-induced dislocation emission (AIDE), where adsorption of hydrogen at crack tips is responsible for hydrogen embrittlement [22]. He further proposed that adsorbed hydrogen weakens the interatomic bond at the crack tips thereby facilitating the nucleation of dislocation and promoting crack growth by localized plastic flow. He based his model on fracture surfaces and compared liquid metal embrittlement (LME) fracture surfaces to the ones obtained from hydrogen embrittlement. LME is attributed to adsorption of liquid metal atoms on the surface of a solid metal, weakening the atomic bond and causing brittle fracture. Due to similarities in the fracture surfaces, he proposed that this could also be the reason for hydrogen embrittlement. Lynch also observed hydrogen embrittlement at very high velocities (up to 1mm/sec), which could not be attributed to mechanisms where hydrogen transport is important (HEDE and HELP).

An important thing to note from this literature review is that hydrogen embrittlement is not completely understood. Several different models have been proposed and the mechanism is very sensitive to the test procedure. High hydrogen pressure and excessive cathodic charging can lead to hydride formation in many metals, while high strain rates can lead to no observation of hydrogen embrittlement [22, 26]. This complexity may be the reason for why hydrogen embrittlement is not completely understood.

2.5. Alloy 718 and Alloy 725

2.5.1. Microstructure

Both Alloy 718 and Alloy 725 are precipitation-hardened alloys. In addition to different kinds of carbides, there are mainly three different precipitates affecting the mechanical properties of the alloys. Gamma prime (γ') and gamma double prime (γ'') are the main strengthening precipitates in both alloys. In addition, a delta phase (δ) is often present. γ'' is an intermetallic compound with a stoichiometric composition as Ni_3Nb and a body-centred tetragonal (BCT) crystal structure[27]. γ'' is, by volume, the major intermetallic phase in both Alloy 718 and Alloy 725 [28, 29]. The amount of γ'' will however vary with

the heat treatment of the material. γ' has a stoichiometric composition as Ni_3(Al, Ti) and the crystal structure is best described as cubic ($L1_2$)[30]. Both phases contribute to the strength via coherency strengthening. The lattice misfit of γ'' and γ' with the matrix is 2,08% and 0,407% respectively [28]. This gives a higher strength contribution from γ''. The kinetics of γ' formation is therefore retarded by adding Nb and reducing the Ti/Al content[31].

When the γ'' is overaged, a more stable δ phase will form. This phase is often found at grain boundaries and is recognized by its needle-shaped morphology. Its composition is also Ni_3Nb, but it has an orthorhombic (DO_a) structure. This phase lower the hardenability and causes some embrittlement of the material[29]. It has some positive effects though, the δ phase precipitates at the grain boundaries and stop grain growth and grain boundary sliding at high temperatures [32].

Blocked shaped carbides will also precipitate homogeneously in the matrix and at the grain boundaries[28]. These are MC carbides, where M is mostly Nb and Ti. They are incoherent with the matrix and gives little precipitation strengthening. They do, on the other hand contribute to the mechanical properties in the same way as the δ-phase[32].

2.5.2. Composition

Although Alloy 718 and Alloy 725 are quite similar alloys, there are some differences in their composition (see Table 2 and Table 3). The important differences are the carbon, chromium, molybdenum, niobium, aluminium and titanium content. Compared to Alloy 718, Alloy 725 has a reduced carbon, niobium and aluminium content to obtain a better weldability[31], while its chromium (Cr) and molybdenum (Mo) content is increased to get better corrosion resistance[33]. Alloy 725 also has a higher titanium content which affects the γ''/ γ' ratio and increase weldability and precipitation kinetics for the hardening phases [34, 35].

2.5.3. Hydrogen embrittlement of Alloy 718 and 725

As previously mentioned, it has been assumed that Alloy 718 and Alloy 725 is not susceptible to hydrogen embrittlement. Due to recent failures of Alloy 718 and Alloy 725 components[3-5], this assumption has been questioned. Standards have been made to

ensure safe use of this alloy. For example, ISO 15156-3, which limits the hardness of Alloy 718 and Alloy 725 components in sour service condition to 35 and 44 HRC, respectively[36].

A lot of work has been done to try to quantify the hydrogen embrittlement susceptibility of different alloys[28, 37, 38]. Hydrogen embrittlement tests on these alloys have shown no [13], or small reductions of UTS. The ductility has, on the other hand, been greatly affected. Both the effect on ductility and stress should therefore be measured when studying the effect of hydrogen.

The susceptibility of an alloy to hydrogen embrittlement is closely related to the microstructure. Alloys that are generally resistant to hydrogen embrittlement may become susceptible due to wrong heat treatment, welding etc. It is therefore important to understand how the different microstructures and precipitates affect the susceptibility.

Alloy 718 is a complex alloy with many types of heterogeneities. Primary and secondary carbides, phase precipitates, grain boundaries as well as impurities will affect the properties of this alloy [32]. All these heterogeneities can affect the hydrogen embrittlement susceptibility. Reversible traps can behave as sources for hydrogen during deformation while irreversible traps may be initiation points for fracture. Hydrogen will accumulate at the irreversible traps, causing earlier fracture of the precipitates and void formation [14]

As mentioned, there are mainly three important phase precipitates in Alloy 718, namely γ', γ'' and δ. Some research has been done to examine the effect of these precipitates on the hydrogen embrittlement susceptibility of Inconel 718. Liu et al. reported that the percent loss of reduction of area due to hydrogen decreased linearly with the decreasing volume of γ'' but that the δ phase had a much higher effect [39]. There are several reports on the deleterious effect of δ phase on the hydrogen embrittlement resistance [28, 37, 38].

It is widely accepted that there is a correlation between the carbide content and the hydrogen embrittlement sensitivity [39]. Pound stated that due to the high binding energy of carbides and carbonitrides, they will act as irreversible traps of hydrogen [14]. The carbides produced in Inconel 718 is manly NbC, but also TiC and carbonitrides [32, 40]. These primary carbides will precipitate at the grain boundaries and may promote intergranular fracture when embrittled by hydrogen. This effect can also be achieved by the δ phase.

The effect of the grain size on the HE susceptibility of superalloys is controversial. It is hard to change the grain size without affecting other parts of the microstructure. Therefore it is difficult to isolate the effect of grain refinement on the HE susceptibility of the alloys. Sjoberg et al.[38] examined, among other things, the effect of grain size on HE sensitivity off Alloy 718 using slow strain rate testing (SSRT) on pre-charged specimen. They found that a small grain sized microstructure was more susceptible than a coarse grained microstructure. They argued that since grain boundaries are often favourable sites for hydrogen segregation due to impurities and phase precipitates, a finer microstructure gives more grain boundary area and more sites where hydrogen can pile up, thereby increasing the hydrogen sensitivity. This theory was contradicted by the work of Lillard et al.[41]. They preformed fracture toughness tests on two different microstructure and found that the coarse grained were more susceptible than the fine-grained microstructure. They proposed that a coarser grain structure gives fewer sites where impurities can segregate, giving a higher concentration of segregates at the grain boundaries. A higher concentration of grain boundary sergeants will increase the HE susceptibility of the material.

Compared to Alloy 718, little literature exists on the HE susceptibility of Alloy 725. Alloy 725 has been sour service tested, but cathodic hydrogen embrittlement has not been a subject of research. Hibner et al. found that according to NACE TM0177 sulfide stress cracking test[42], Alloy 725 is immune to hydrogen embrittlement. Recent work contradicts this conclusion. Shademan et al. [3] identified hydrogen induce cracking as a possible reason for failure in a subsea component.

2.5.4. Hydrogen diffusion in Alloy 718

An important factor of how susceptible a material is to hydrogen embrittlement is the diffusivity of hydrogen in the material. A low diffusivity will increase the time to achieve critical hydrogen concentrations in the material. Doing some diffusion analyses will therefore be of great value to any work done on hydrogen embrittlement. The diffusivity will, as mentioned, be dependant of the traps and heterogeneities in the material. These must therefore be accounted for when analysing the diffusion hydrogen. W. M. Robertson[43] estimated the diffusivity of hydrogen in Alloy 718, disregarding the effects of trapping. He did this by performing a permeation test. In his work, he found the diffusion coefficient of hydrogen in Inconel 718 as shown in equation (13.). The results also revealed that the diffusion coefficient was relatively unaffected by the heat treatment, but that the solubility was changed.

$$D\left[\frac{cm^2}{s}\right] = 1.07\times10^{-2}\exp\left(\frac{-11{,}900}{RT}\right) \qquad (13.)$$

Inserting 293 K and the gas constant to equation (13.) gives a diffusivity of 1,42 x 10^{-15} m/s^2. This seems to coincide well with other reported values[44]. Reported diffusivities of H in super duplex stainless steels (SDSS) and duplex stainless steels (DSS) varies between 1.8 x 10^{-12} and 4,6 x 10^{-16} m/s^2 [45]. The reason for this large interval is that the diffusivity in these alloys is very dependent on the austenite spacing. One should however expect that the diffusivity in SDSS and DSS is slightly higher than in Alloy 718 due to the presence of ferrite phase. Hydrogen diffusion in an Austenitic stainless steel was measured to 1,8-8 x 10^{-16} [45]. This alloy has the same FCC structure as Alloy 718. The difference in diffusivity must therefore be attributed to alloying elements and other microstructural effects. It should be noted that these values are obtained by permeation techniques, which are very sensitive to small experimental alterations. This may be one of the reasons for the variations in the reported diffusivities for a given material.

3. Experimental and material

3.1. Material

Both materials used in this thesis were forged qualities. The manufacturer of the material supplied a datasheet for both alloys. Key data from these data sheets are given in Table 1, while the composition of the two alloys are given in Table 2 and Table 3. The Alloy 718 material was received as a part of a forged bolt, while the Alloy 725 material was received as a forged ring. Since the material properties may vary through the cross section of the bolt, the Alloy 718 samples were extracted at an equal distance from the centre, as shown in Figure 13. Figure 12 show how the Alloy 725 samples were extracted.

Table 1: Key properties found in the material datasheet

Material	YS (MPa)	UTS (MPa)	Grain Size (ASTM standard)
Alloy 718	944,6	1289,3	4 (predominantly)
Alloy 725	923,9	1275,5	3,5-4,5

Table 2: The composition of Alloy 718

Element	**C**	**Si**	**Mn**	**P**	**S**	**Cr**	**Mo**	**Ni**	**Al**
Wt %	0,021	0,05	0,05	0,007	0,0003	17,77	2,69	53,88	0,48
Element	**B**	**Co**	**Cu**	**Nb**	**Pb**	**Sn**	**Ti**	**Bi**	**Ca**
Wt %	0,0035	0,17	0,04	5,02	0,0001	0,0004	0,97	<3E-05	0,0001
Element	**Mg**	**Se**	**Ta**	**Fe**	**Nb+Ta**				
Wt %	0,0006	0,0001	0,004	Bal	5,024				

Table 3: The composition of Alloy 725

Element	**C**	**Si**	**Mn**	**P**	**S**	**Cr**	**Mo**	**Ni**	**Al**
Wt %	0,014	0,04	0,04	0,003	0,0008	20,76	7,87	57,87	0,31
Element	**Co**	**Cu**	**Nb**	**Ti**	**Ca**	**Mg**	**Ta**	**Fe**	**Nb+Ta**
Wt %	0,04	0,01	3,54	1,55	0,0008	0,0002	0,005	bal	3,545

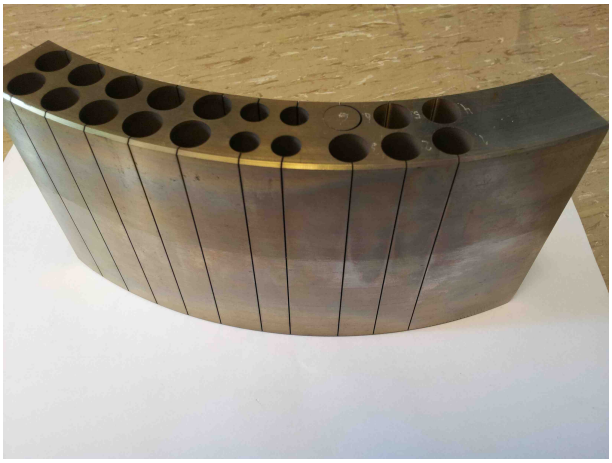

Figure 12: A picture of how the Alloy 725 samples were extracted from the material.

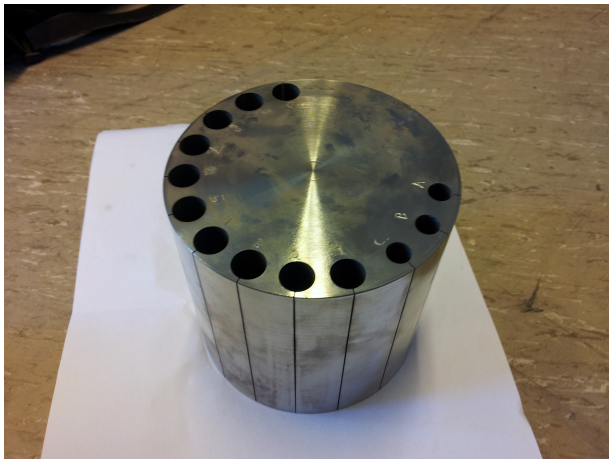

Figure 13: A picture of how the Alloy 718 samples were extracted.

3.2. Mechanical testing and microstructure examination

The mechanical properties found in the datasheet for each metal, was examined using common metallographic techniques. Samples for tensile testing and microstructure examination was prepared. The tensile samples were tested according to "Norsk Standard for tensile testing"[46] at the department of materials technology. Three round samples were tested to get representative values. The dimensions of the tensile samples are given in Figure 14.

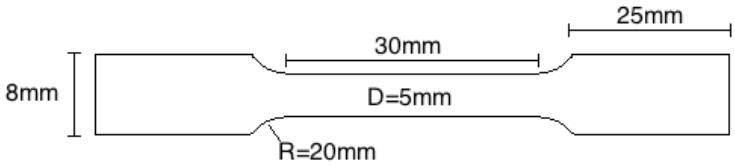

Figure 14: Dimensions of the tensile specimen.

To be able to confirm that the grain size given in the material data sheet was roughly correct, the microstructure was studied in an optical microscope. Samples were cut from the tensile bars and moulded in Epoxy. The sample surfaces were then prepared with the following steps to reveal the microstructure:

- Grinding on 800 and 1200 grit paper.
- Mechanical polishing with 3 µm and 1 µm particles.
- Etched in Kalling's nr 2 etch prepared according to ASTM standard E407-07[47] . The samples were etched until the microstructure was revealed (up to 8 minutes).

The samples were then examined in an optical microscope. The grain size was determined by a planimetric procedure according to ASTM standard E112[48].

3.3. HISC testing

The setup for the HISC testing is based on a procedure developed for HISC testing of Duplex and Super Duplex stainless steel (DSS and SDSS)[6]. As described in chapter 3.3.1, the pre-charging procedure was changed to compensate for the different diffusion rates in nickel alloys and SDSS. In addition, constant load tests were preformed to find a safe load.

The test matrix for the HISC testing can be divided into two parts. In the first part, a critical stress for fracture due to hydrogen embrittlement will be found by stepwise increasing load testing. The second part will consist of trying to verify this critical stress. To get a better overview, the parts can be further divided into these steps:

Part 1:
Step 1: Pre-charge 5 tensile bars of each alloy for 5 days as described in the next chapter.
Step 2: Measure the initial diameter of the Cortest proof ring and the diameter of the sample. Place one bar in each chamber of the Cortest proof rings. Fill the chambers with 3,5% NaCl electrolyte and polarize the samples to 1050 $mV_{Ag/AgCl}$. Load the bars to 86% of the YS. The bars will stay at this load for 10 days. It will be adjusted for creep once every day.
Step 3: After 10 days have past the load will be increased every day until fracture. The load is increased with 8% of YS the two fist days, then increased by 4% of YS until fracture occurs. The results will then be studied and a critical stress level will be found and used for the next part of the experiment. Two samples of each alloy will be stored in a freezer and sent to hydrogen measurements.
Step 4: Use a load cell to verify the fracture loads calculated by the conversion charts.

Part 2:
Step 1: Pre-charge 3 tensile bars of each alloy for 5 days as described in the next chapter.

Step 2: Measure the area of each tensile bar. Use this area to calculate the load needed to get a stress corresponding to 95% of the fracture stress found in part 1. Use the load cell to find the deflection need to obtain this load.
Step 3: Place one bar in each chamber of the Cortest proof rings. Fill the chambers with 3,5% NaCl electrolyte and polarize the samples to 1050 $mV_{Ag/AgCl}$. Load the bars to 95% of the critical stress level obtained in part 1, and leave it there for 30 days at room temperature.

Figure 15 shows the dimensions of the tensile bars used for the HISC testing. These dimensions are retrieve from NACE standard TM0177[49] with one alteration; the diameter is reduced to 3mm to ensure higher hydrogen concentration over the cross section. Figure 16 shows a picture of the HISC bars.

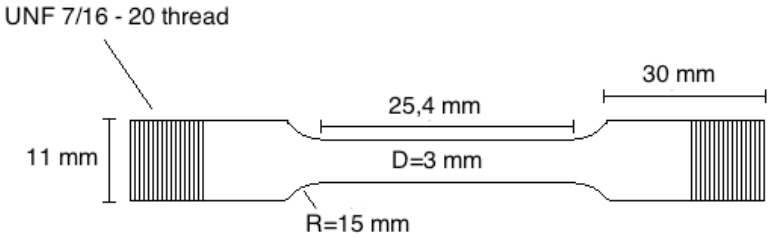

Figure 15: A sketch of the dimensions of the HISC tensile bars.

Figure 16: A picture of the HISC bars after pre-charging.

3.3.1. Pre-charging

In previous work related to this project, samples were pre-charged at 1050 $mV_{Ag/AgCl}$ in a 3,5% NaCl electrolyte at 80°C. These parameters made the pre-charging very time consuming. Another problem was the formation of a black residue on the sample surfaces during pre-charging. A new setup for the pre-charging was therefore developed. The water-based electrolyte was replaced with an electrolyte with a higher boiling point. In this way the temperature during pre-charging could be increased. The electrolyte used for the new setup was a 2:1 mixture of Glycerol and 85% H_3PO_4 (Ortho-phosphoric acid). The stability of this electrolyte was tested up to 150°C.

The new setup included $Hg/HgSO_4$ reference electrodes, a multichannel Gamry potentiostat, a round-bottomed glas flask with accompanying caps, platinum wires for the counter electrodes and an oil bath with a temperature regulator (see Figure 17). Two HISC specimens was attached to platinum wires and added through the middle hole of the flask. Platinum counter electrodes were inserted on each side. A tube was inserted through one of the caps to maintain contact with the reference electrode. The flask and tube were then filled with the electrolyte and lowered into the oil bath. Finally, all electrodes were connected to the potentiostat.

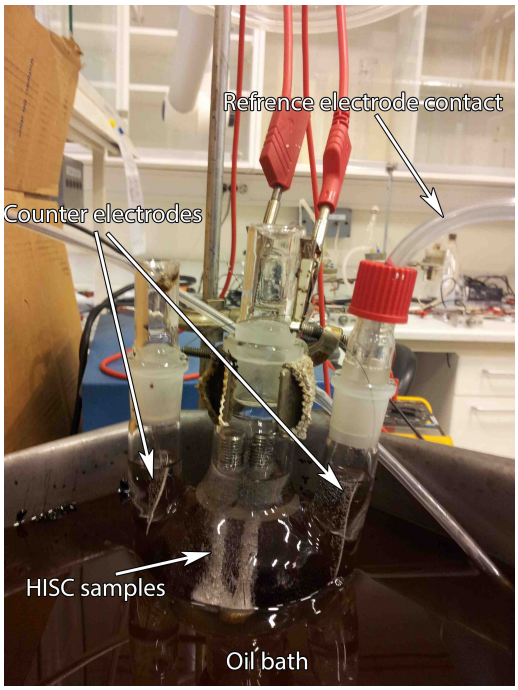

Figure 17: A picture of the pre-charging setup. The samples in this picture are polarized to 1050 $mV_{Ag/AgCl}$ and completely covered in hydrogen bubbles. The container for the pre-charging cell is submerged in an oil bath.

All HISC tensile bars were washed with acetone before pre-charging. Afterwards, they were connected to the potentiostat as working electrodes and submerged in the electrolyte. They were polarized to -1050 $mV_{Ag/AgCl}$ at 120°C. All samples were pre-charged for 5 days. The electrolyte gradually turned dark brown during the pre-charging. It was therefore changed once every second day.

3.3.2. Cortest proof rings

The HISC testing itself was preformed in Cortest proof rings. Twelve of these rings are installed in the SINTEF Corrosion Laboratory. These are actually used for sulphide stress cracking (SSC) tests[49], but can easily be adapted to include polarization of the samples. The setup includes a stainless steel ring, which controls the load on the specimen, a sealed acrylic glass chamber for the electrolyte, a potentiostat and a timer. A counter and an Ag/AgCl reference electrode was inserted through the holes meant for inlet and outlet of H_2S gas. The modifications are shown in Figure 18.

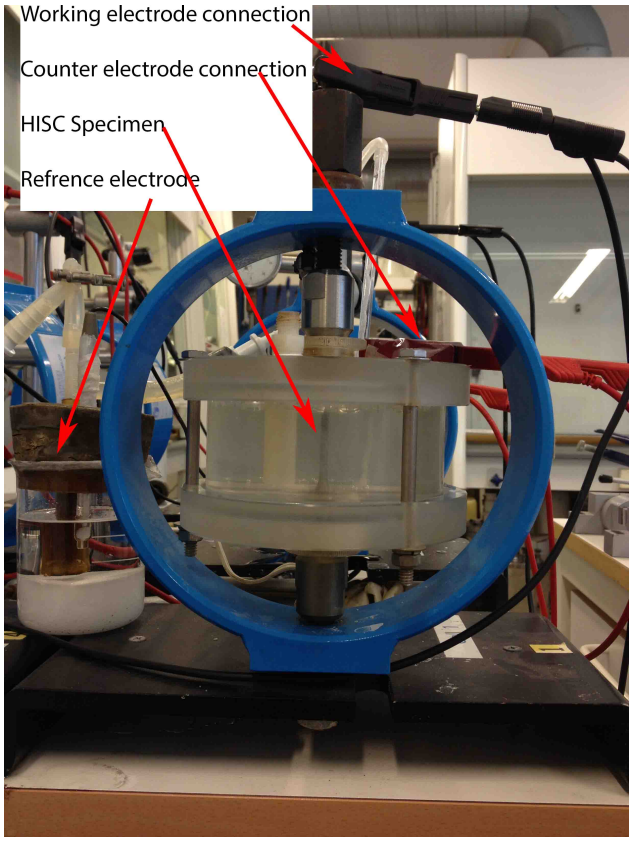

Figure 18: A platinum counter electrode and an Ag/AgCl reference electrode is fitted into the setup as shown in the picture.

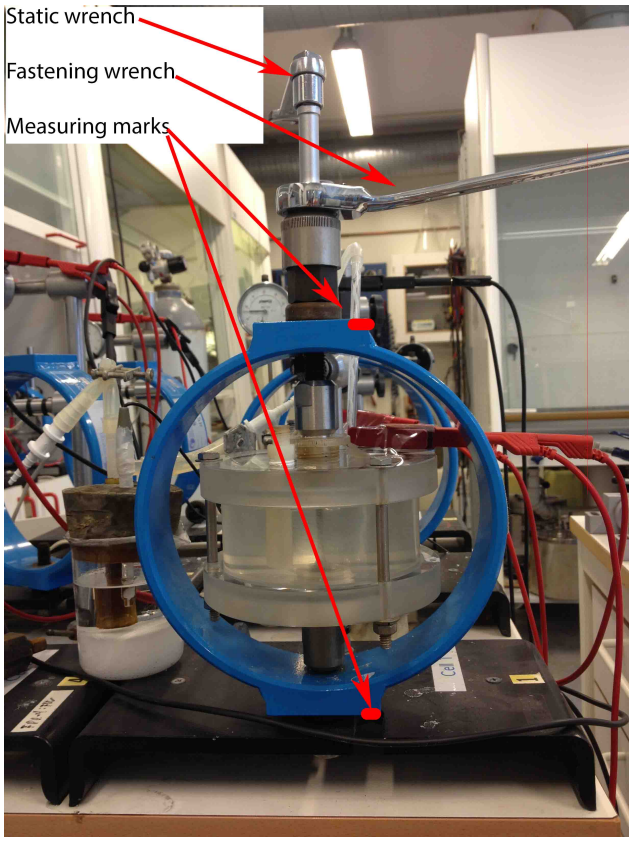

Figure 19: The load is adjusted by turning the fastening wrench. The diameter is measured over the measuring marks by a calliper.

The diameter of the tensile specimen and the Cortest rings at zero load was measured by a calliper before each test. These measurements were inserted into the conversion chart to calculate the ring diameter for the desired force. The same calliper was used to measure the ring diameter during loading. A nut on the top of the Cortest proof ring was tightened to reduce the ring diameter and thereby increasing the load on the specimen. The wrenches and the measuring points are shown in Figure 19. If a specimen broke during constant load a sensor connected to the ring and a timer was used to determine when it broke.

The rings diameter was measured by a calliper with a reading of 0,01 mm. The diameter values given by the conversion chart, were therefore rounded of to the hundred of a millimetre. The applied load would therefore deviate slightly from the desired load. After testing, a goal seeking method was used in Excel to find the exact load corresponding to the deflection with two decimals.

A load cell was used to find the exact load corresponding to the deflections at fracture. The load cell was inserted into the ring and loaded until the desired deflection was obtained. The load was then read of the load cell. This was preformed three times for each ring and deflection to get an accurate reading. Figure 20 shows how the load cell was inserted into the ring.

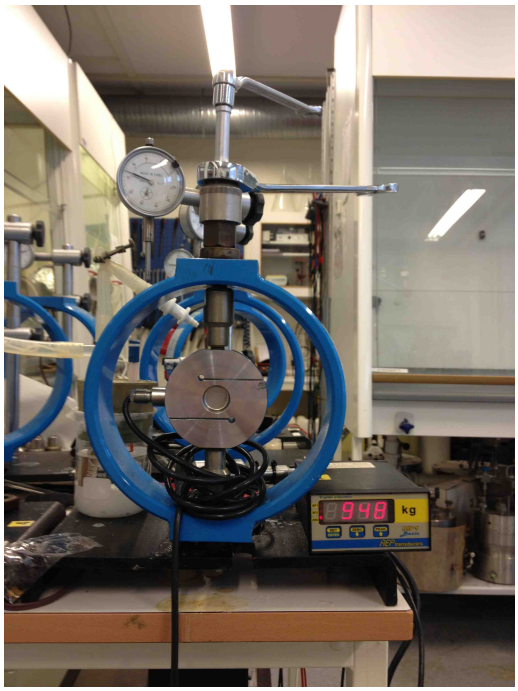

Figure 20: Shows how the load cell was inserted into the Cortest proof rings.

3.3.3. Reference electrode conversions

In this thesis, three different reference electrodes were used. $Hg/HgSO_4$ were used for the pre-charging, whiled Ag/AgCl and saturated Calomel electrodes were used in the Cortest proof rings. The values presented in Table 4 made it possible to work with different reference electrodes and relate the potentials to each other.

Table 4: The values given here were used to convert potentials from one reference electrode to another. Gamry Instruments supplied these values.

Reference electrode	E vs NHE (V)	E (mV) corresponding to -1050 $mV_{Ag/AgCl}$
Ag/AgCl (Saturated KCl)	0,198	-1050
Saturated Calomel	0,241	-1093
$Hg/HgSO_4$	0,654	-1506

3.4. Fracture surface examination

After the tensile testing and HISC testing, the fracture surfaces were washed in acetone, dried and examined in the Zeiss Supra LVFESEM located at the department of materials technology. The fracture morphology was studied to determine the mechanism of the fracture. An effort was made to try to measure how near the centre the brittle features existed. This proved to be impossible since there was no clear transition from brittle to ductile features.

The RA was measured for each tensile bar and HISC bar. This was used to calculate the reduction in reduction of area (RRA), and thereby quantifying the effect of hydrogen on the ductility of the two alloys. A calliper was used to determine the diameter before after after fracture.

4. Results

4.1. Pre-charging

The potentiostat used for the pre-charging logged the current and the potential during the time of the charging. These values were imported to Excel and used to make graphs as show in Figure 21 and Figure 22. Large fluctuations in the current were observed. The three peaks in the graphs occurred due to the change of electrolyte and the following temperature drop. The counter electrodes were removed and washed before they were reinserted into the pre-charge chamber. In this way, the distance between the anode and the cathode was altered, which did also affect the current. It also seems as the resistance in the electrolyte gradually increased during the pre-charging. The pre-charge graphs for the rest of the samples are included in Appendix A.

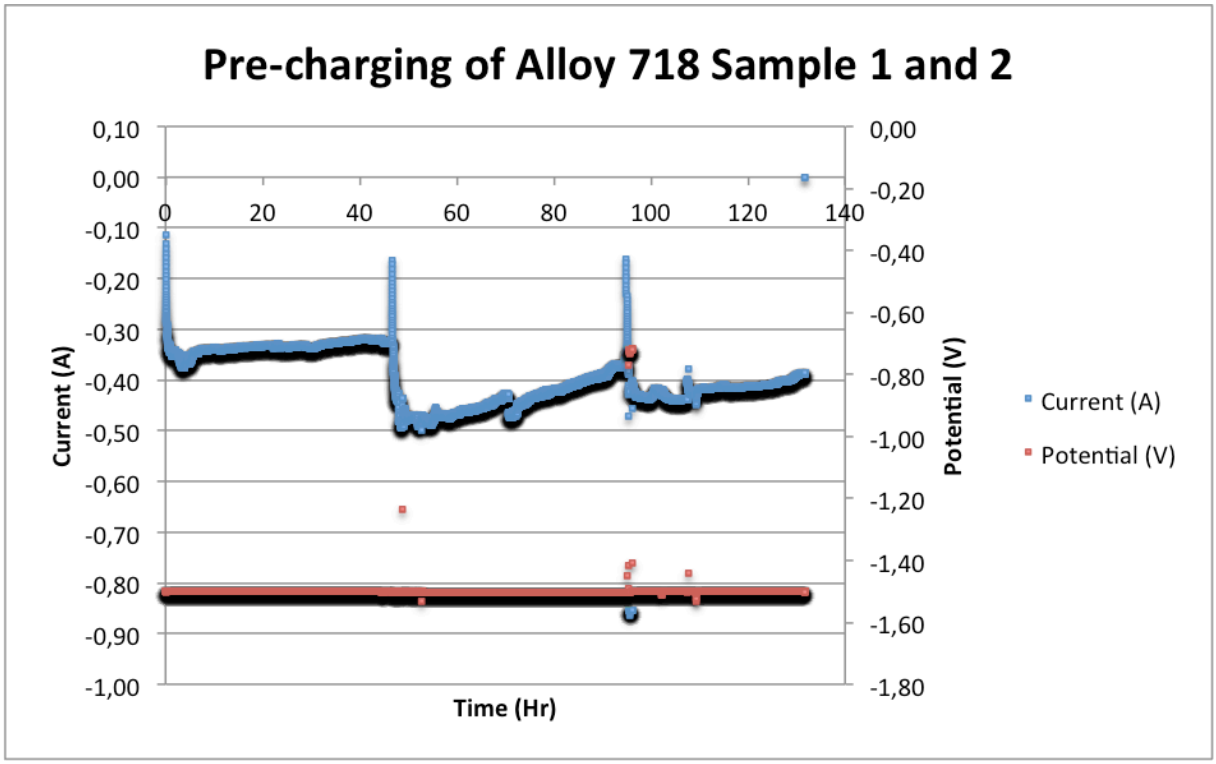

Figure 21: A current and potential plot for HISC sample 1 and 2 of the Alloy 718 material. The potential is measured against a $Hg/HgSO_4$ reference electrode.

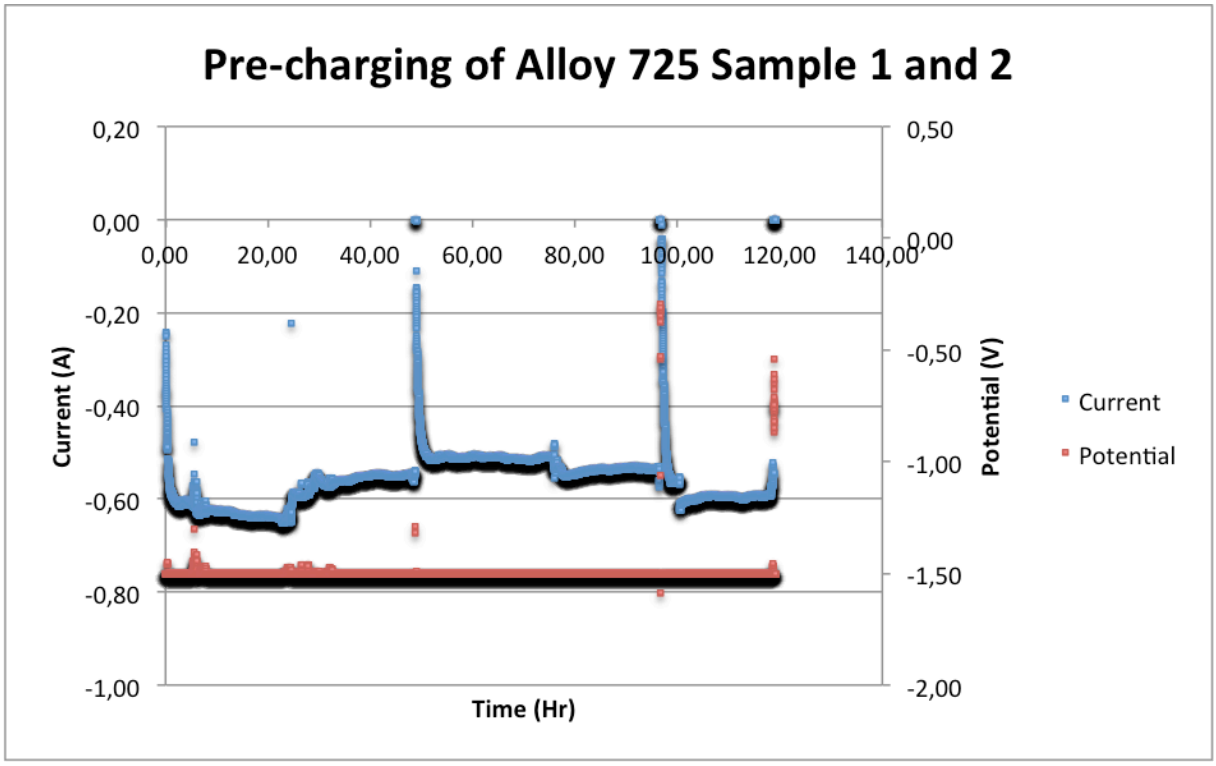

Figure 22: A current and potential plot for HISC sample 1 and 2 of the Alloy 725 material. The potential is measured against a $Hg/HgSO_4$ reference electrode.

Because of the large fluctuations in the pre-charging graphs, the average current was calculated for each pre-charge. The result is presented in Table 5

Table 5: A table showing the average current during pre-charging

Average current during pre-charging		
Alloy 718	**Sample No**	**Current (A)**
	1 and 2	0,395
	3 and 6	0,367
	7 and 9	0,762
	8 and 10	0,504
	4 and 5	0,642
Alloy 725		
	1 and 2	0,556
	3 and 4	0,485
	5 and 6	0,484
	7 and 8	0,43
	9 and 10	0,51

4.2. Tensile testing

Table 6 shows the key data obtained from the tensile testing, while Figure 23 shows the stress-strain curve for specimen No. 3 of both alloys. The lowest value of YS (specimen No. 3 for both alloys) was used in the HISC testing. This was done to obtain conservative results.

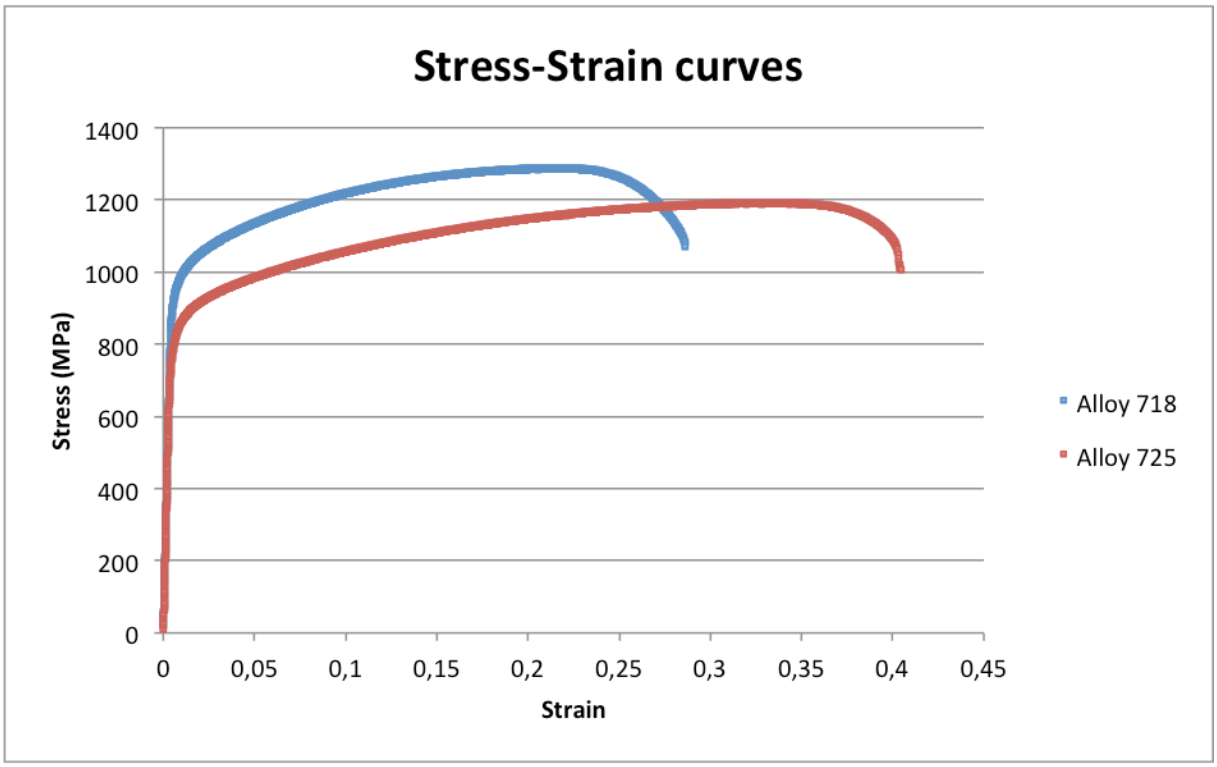

Figure 23: Shows the obtained stress-strain curves for both Alloy 718 and Alloy 725.

Table 6: Results from the tensile testing of Alloy 718 and Alloy 725

Material	Specimen No.	Modulus (GPa)	YS (MPa)	UTS (MPa)	UTS/YS (%)	Strain at break (%)
Alloy 718	1	203,6	953,7	1301,8	136,5	29,8
	2	214,0	954,3	1301,7	136,4	26,2
	3	208,1	943,1	1288,3	136,6	28,6
Alloy 725	1	207,3	818,5	1213,1	148,2	42,1
	2	202,8	838,5	1217,1	145,2	36,4
	3	203,0	805,1	1192,4	148,1	40,4

4.3. Grain size measurements

Figure 24 and Figure 25 show microstructural images of Alloy 718 and Alloy 725, respectively. Some grains were hard to differ from one another, so help lines were drawn in. The grain size was then calculated according to ASTM E112[48].

$$Alloy\ 718: D = 85\ \mu m$$
$$Alloy\ 725: D = 108{,}5\ \mu m$$

These grain sizes correspond to an ASTM standard grain size of 3.0 for Alloy 725 and 4.0 for Alloy 718.

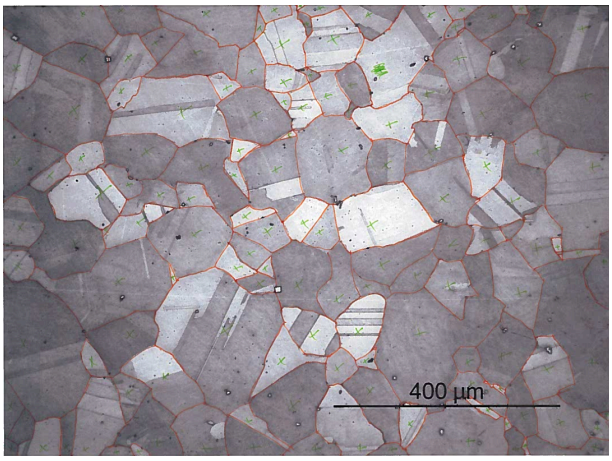

Figure 24: Optical microscope image of Alloy 718 with drawn in help lines for grain size measurement.

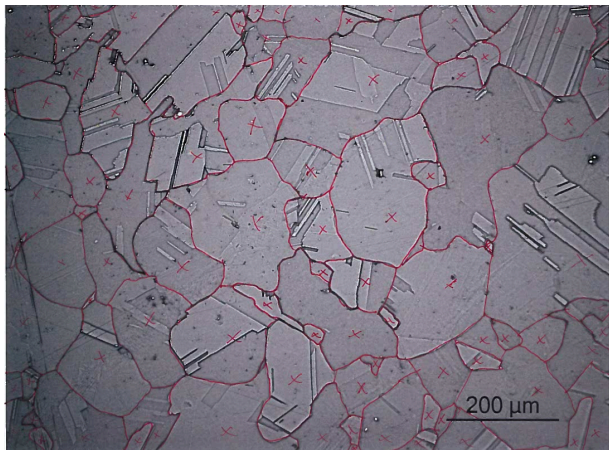

Figure 25: Optical microscope image of Alloy 725 with drawn in help lines for grain size measurement.

4.4. HISC testing – Phase 1

The results from HISC testing Phase 1 are presented in Table 7 and Table 8. The "No fracture" value is the last recorded load where no fracture occurred, while the "Fracture" value is the last recorded load when fracture occured. The load is given as per cent of yield strength. There was a high deviation in the first five samples for Alloy 718. Two more samples were therefore tested. Sample 2 for Alloy 718 broke during loading to 86% of yield due to an error made by the operator. Two samples of each Alloy were stored in the freezer for later hydrogen measurements.

Table 7: Shows key results from the HISC testing of Alloy 718. The no fracture value is the last load where no fracture occurred, while the fracture value is the load where fracture did occur.

Alloy 718					
	Using conversion chart			Using to load cell	
	No fracture (% of YS)	Fracture (% of YS)	Fracture time	No fracture (% of YS)	Fracture (% of YS)
Sample 1	129,23 %	134,08 %	During loading	133,94	137,22
Sample 6	-	-			
Sample 9	108,84 %	113,69 %	Constant load	113,74	118,59
Sample 8	117,41 %	122,36 %	During loading	121,34	126,89
Sample 10	125,19 %	129,99 %	During loading	121,89	127,04
Sample 2	114,35 %	118,19 %	Constant load 1min	121,67	126,89
Sample 5	117,74 %	121,53 %	Constant load 1min	120,26	126,18

Table 8: Key result from the HISC testing of Alloy 725.

Alloy 725					
	Using conversion chart			Using to load cell	
	No fracture (% of YS)	Fracture (% of YS)	Fracture time	No fracture (% of YS)	Fracture (% of YS)
Sample 1	117,31 %	123,43 %	Constant load 17hr	131,83	135,85
Sample 2	118,48 %	121,38 %	During loading	132,92	136,66
Sample 3	117,30 %	123,63 %	During loading	134,74	140,49
Sample 4	109,51 %	115,36 %	Constant load 2 min	132,43	139,11
Sample 5	118,20 %	121,10 %	Constant load 30 min	133,41	135,94

The results in Table 7 and Table 8 are presented in Figure 26. The “No hydrogen” values are the results obtained from the tensile testing, while the “Hydrogen” values are those obtained from the HISC testing. The high standard deviation for Alloy 718 is mainly due to the sample 1 and sample 3. If these two are excluded from the calculations, the deviation is greatly reduced. This is shown in Figure 27.

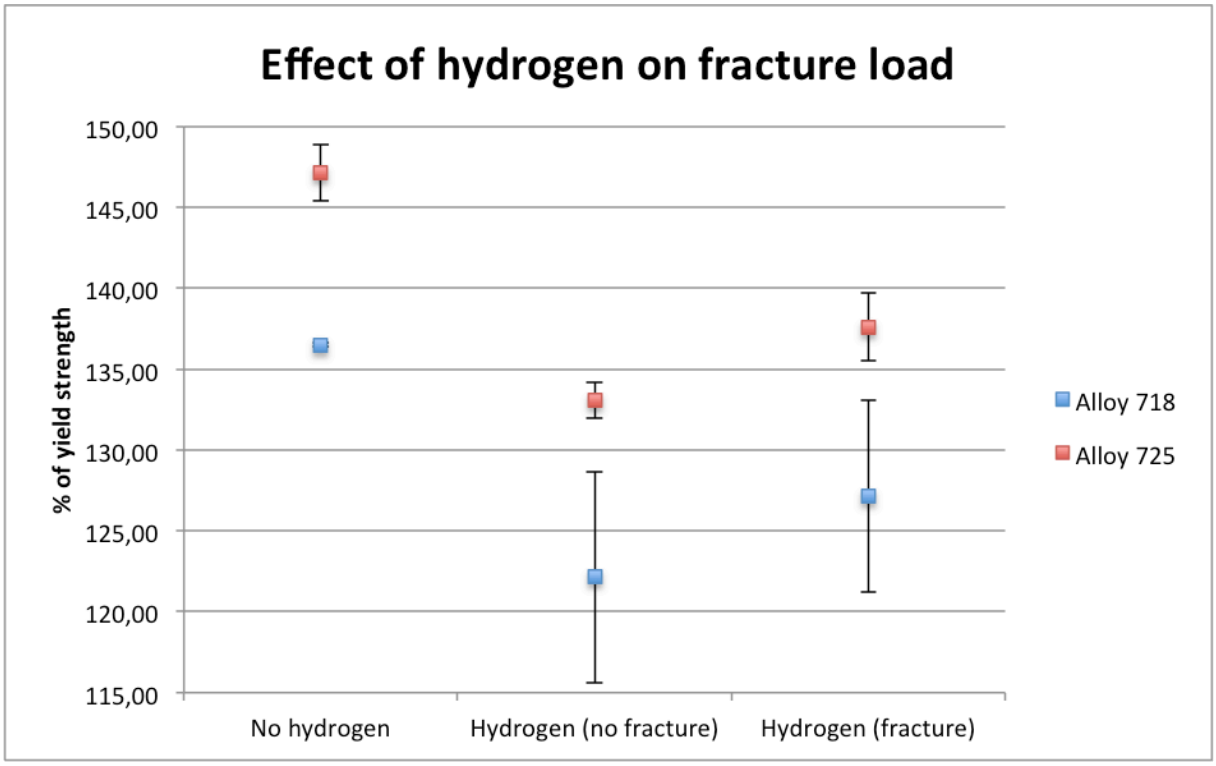

Figure 26: Illustrates the effect of hydrogen on the fracture load of Alloy 718 and Alloy 725. All results from the HISC testing are included.

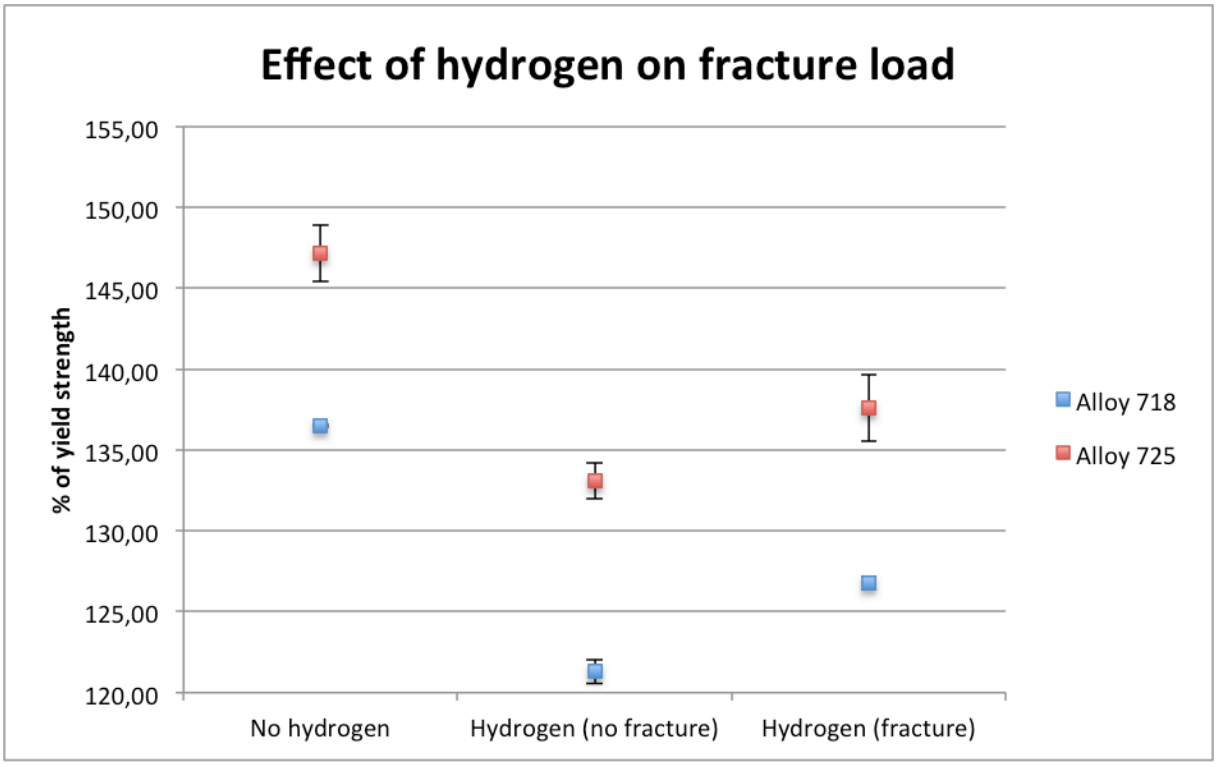

Figure 27: The same figure as Figure 26, only without Alloy 718 samples 1 and 3. This is the reason for the reduced standard deviation.

4.5. HISC testing – Phase 2

Three samples of each alloy were loaded to 95% of the "fracture" value obtained from Phase 1 of the HISC testing. None of the Alloy 718 samples failed, while all Alloy 725 samples failed. New pre-charged Alloy 725 samples were therefore loaded to 90% of the "fracture" value. None of the samples failed during the 30 days at this load. The results are summarized in Table 9.

Table 9: A table displaying the results from the constant load testing.

Alloy 718	Sample Nr	Stress (% YS)	Failure (Yes/No)	Time to failure (Hr)
	1	120,4 %	No	-
	2	120,4 %	No	-
	3	120,4 %	No	-
Alloy 725				
	1	130,7 %	Yes	48,9
	2	130,7 %	Yes	52,8
	3	130,7 %	Yes	86
	4	130,7 %	Yes	428
	5	123,8%	No	-
	6	123,8%	No	-
	7	123,8%	No	-

4.6. Fracture surface characterization

The samples from the standard tensile test experienced necking and failed in a very ductile manner. This could be observed on a macroscopic scale (see Figure 28).

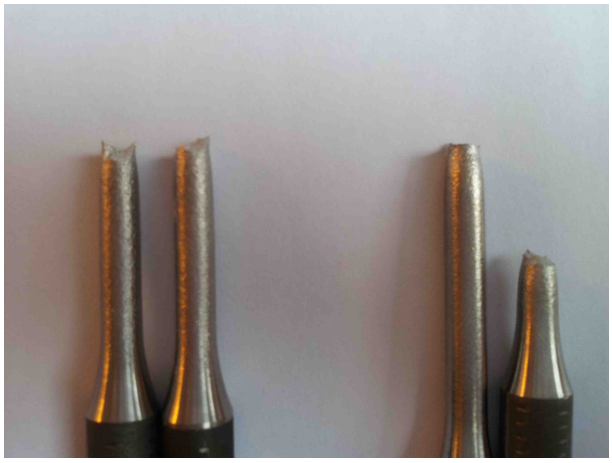

Figure 28: A picture of the tensile bars after fracture. On the left is one of the Alloy 725 bars, while the one on the right is Alloy 718.

4.6.1. Alloy 718

Both the fracture surfaces from the standard tensile test and the HISC test were examined. Already on a macroscopic scale, one could observe a loss of ductility (no necking) in the HSIC test. The loss of ductility was also observed on the fracture surfaces. The fracture surface from the standard tensile test is presented in Figure 29 while the fracture surface from one of the HISC tests is presented in Figure 30.

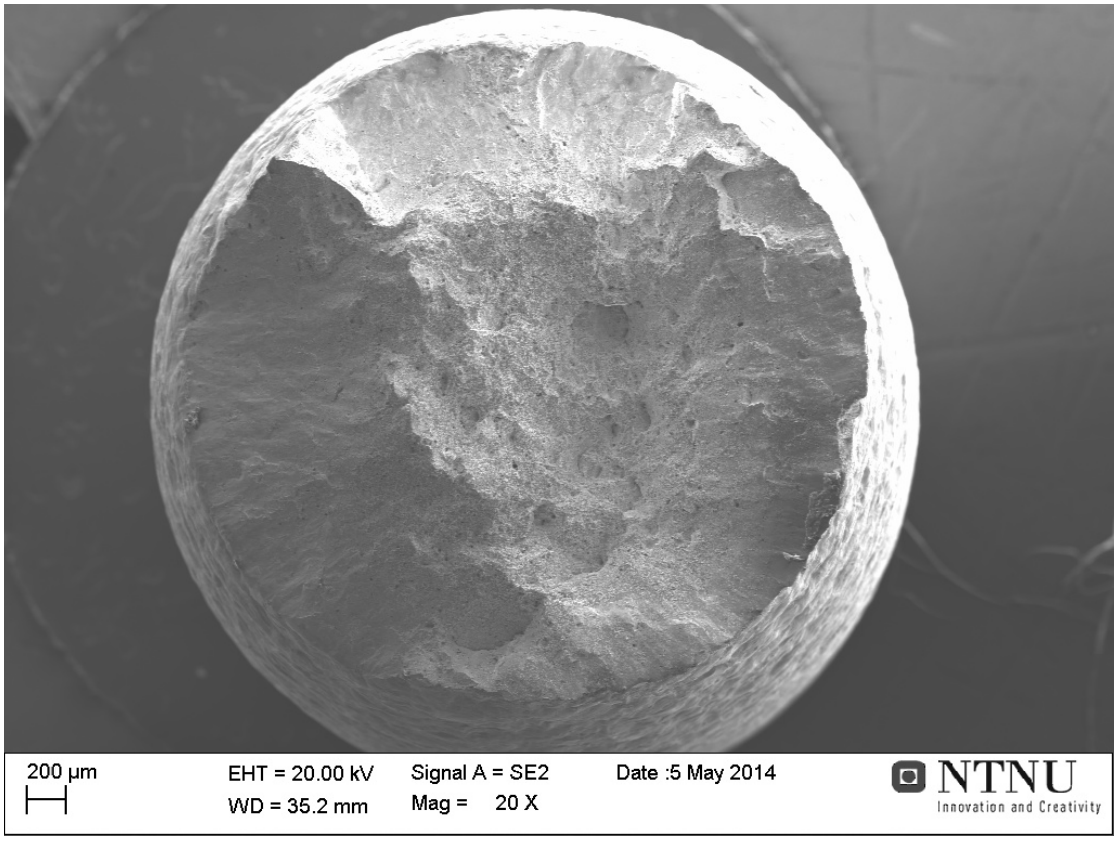

Figure 29: The fracture surface from the standard tensile test of Alloy 718.

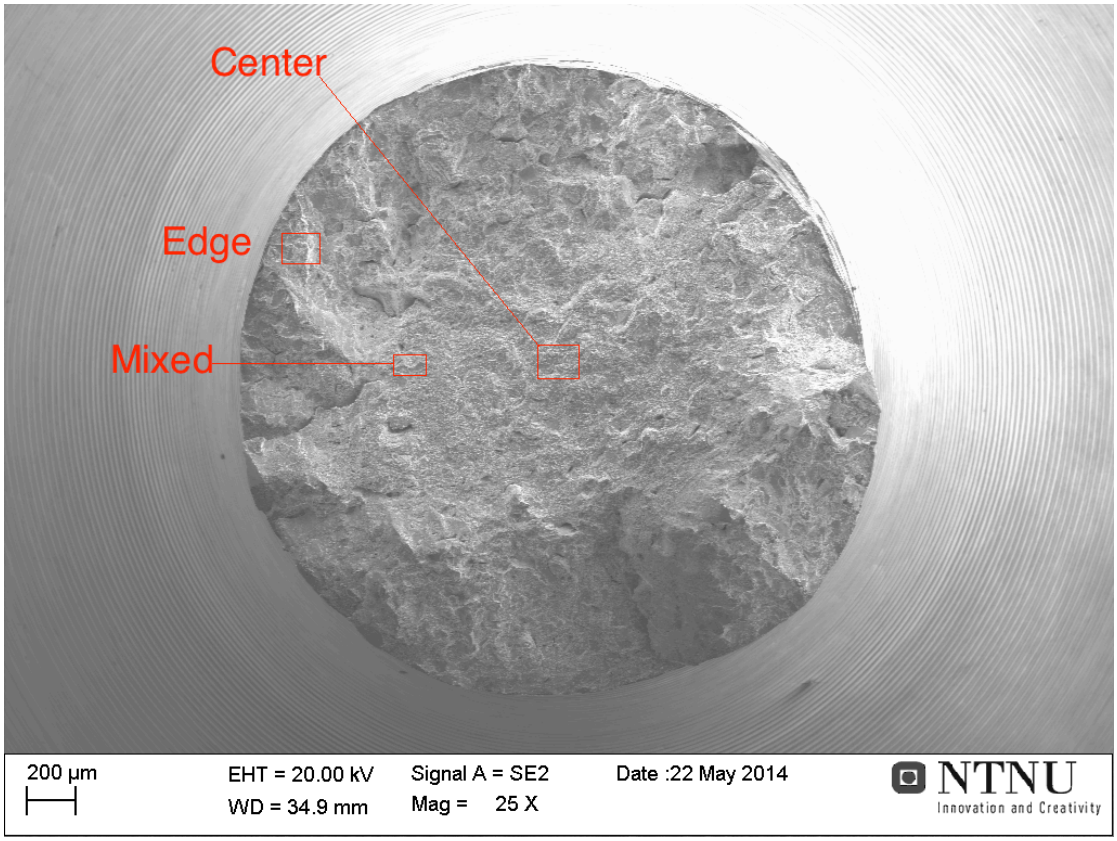

Figure 30: The fracture surface from HISC test of Alloy 718. The marked squares are areas where the next photos are taken.

A closer look at the standard tensile test fracture surface revealed only ductile features. The HISC samples revealed, on the other hand brittle features near the edges. Pictures at higher magnifications of the HISC samples are included in Figure 31 to Figure 35. Figure 31 and Figure 32 show the ductile features in in centre of the fracture surface. Particles can be observed in some of the dimples. Figure 33 shows the brittle fracture features on the edge of the fracture surface. At higher magnifications some river patterns could be observed indication transgranular fracture (Figure 34). The last image, Figure 35, shows an area with both ductile and brittle features.

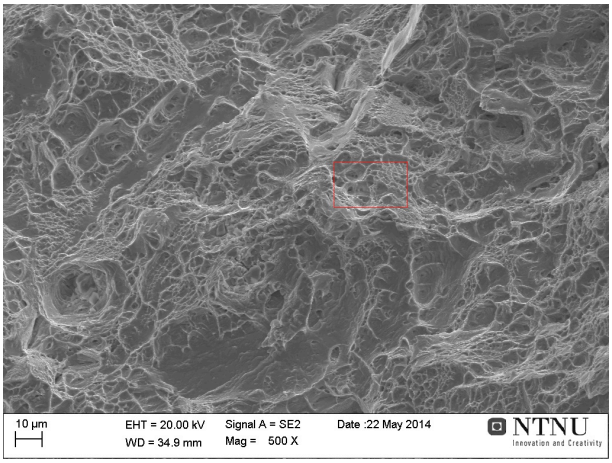

Figure 31: A closer look at the centre of the HISC fracture surface. The focus of this picture is marked with a red square and called "centre" in Figure 30.

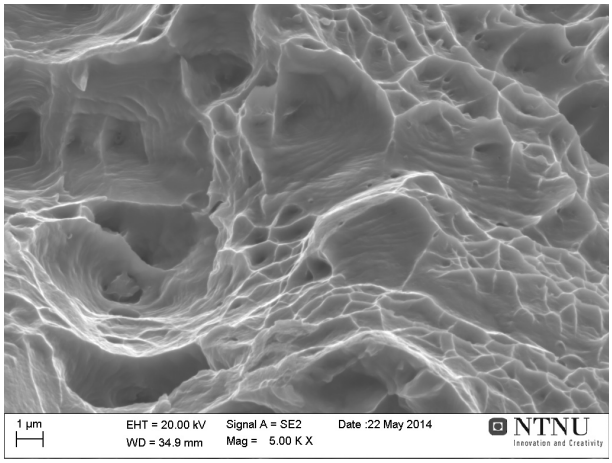

Figure 32: This is a closer look on the marked area in Figure 31.

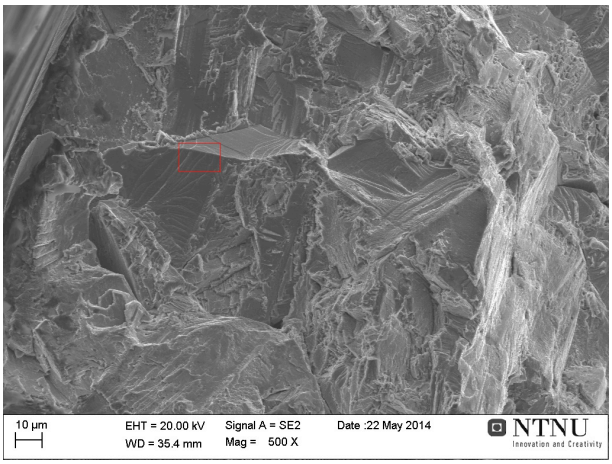

Figure 33: a closer look at the square called "edge" in Figure 30.

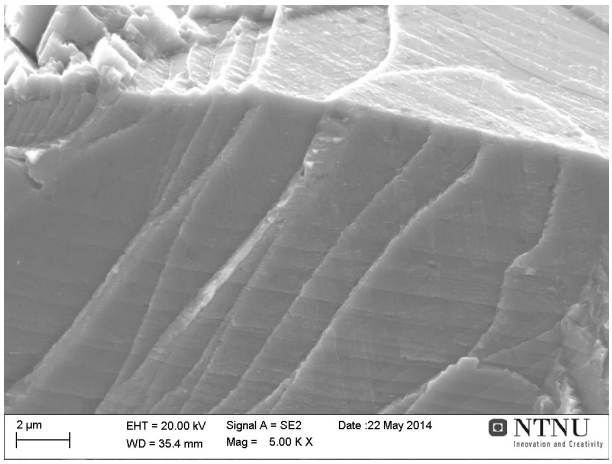

Figure 34: This is a closer look at the red square marked in Figure 33.

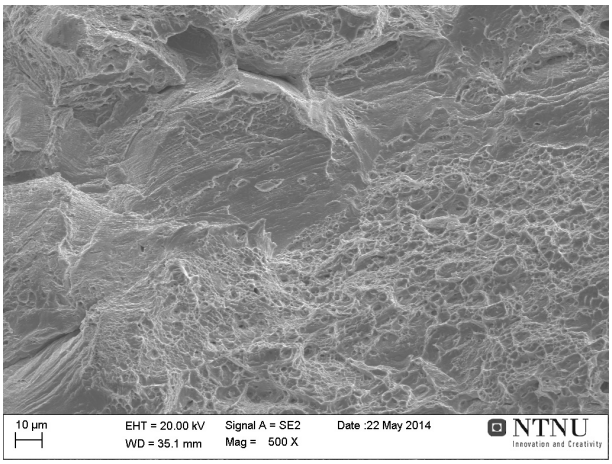

Figure 35: A closer look at the square called "mixed" in Figure 29.

4.6.2. Alloy 725

The same fracture surface examination was preformed on the Alloy 725 samples. Picture of the standard tensile test fracture surface is included in Figure 36, while an overview of the HISC sample fracture surface is included in Figure 37.

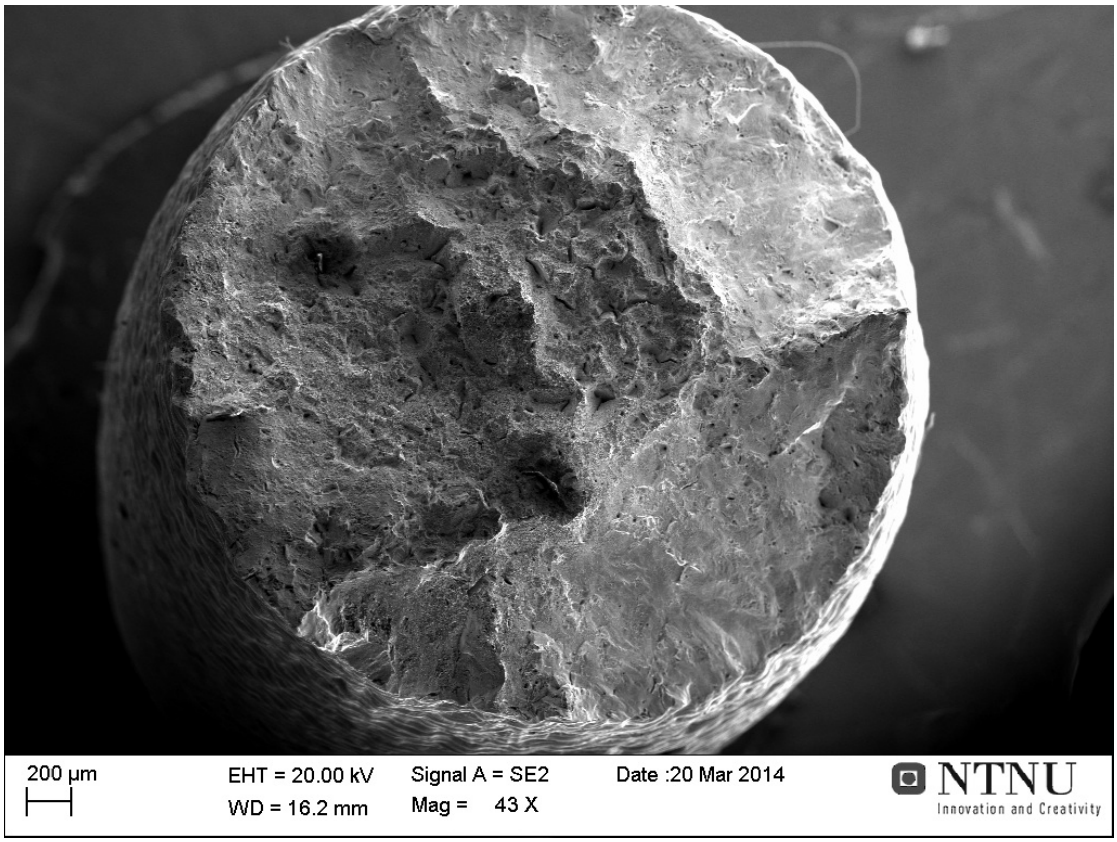

Figure 36: This picture was taken of the fracture surface from one of the standard tensile tests preformed on Alloy 725.

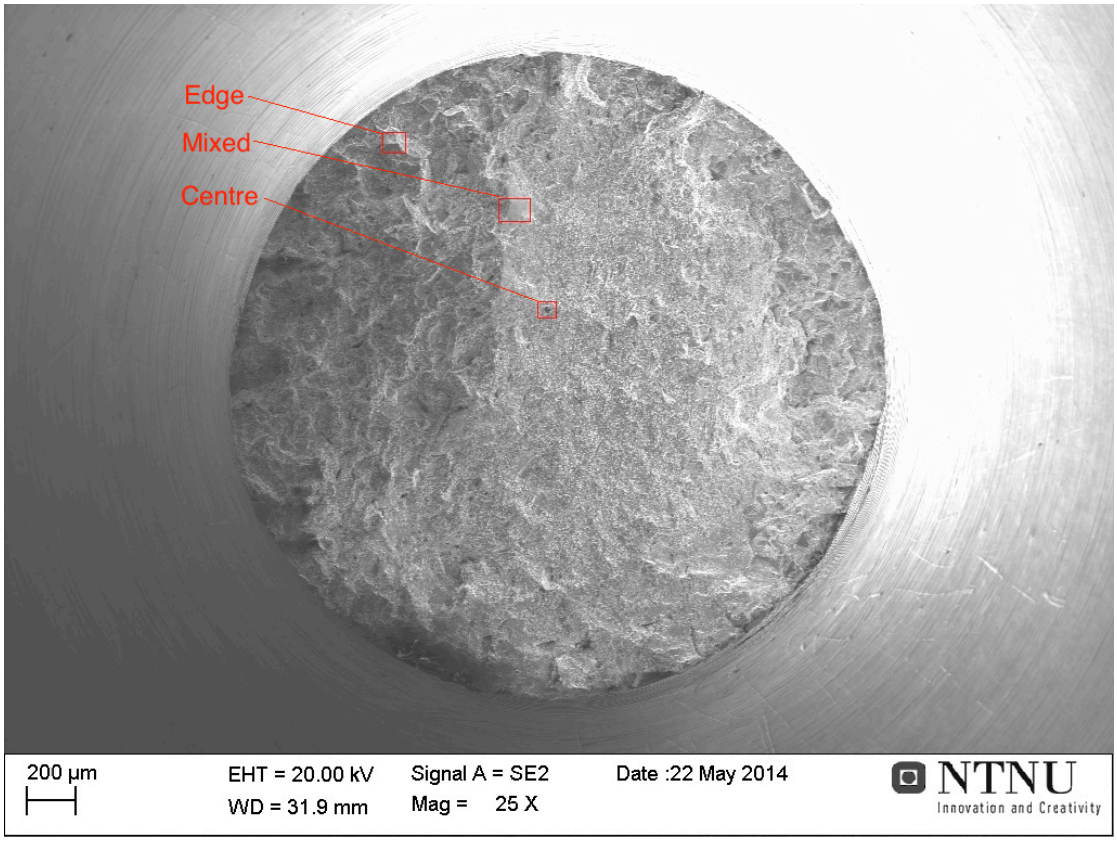

Figure 37: This is an overview photo of a fracture surface from one of the HISC tests of Alloy 725.

As for Alloy 718, the standard tensile test fracture surface revealed only ductile features. The fracture surfaces of the HISC sample revealed similar features as the HISC fracture surfaces of Alloy 718. Dimples were observed near the centre, while transgranular brittle features dominated near the edge. The red squares in Figure 37 marks areas where higher magnification pictures were taken. These are included in Figure 38 to Figure 42. Figure 38 and Figure 39 show the dimples found in the centre of the fracture surface. Indicating a ductile mechanism in the centre where the hydrogen concentration is lowest. Figure 40 and Figure 41 show higher magnification images at the edge of the fracture surface. Here brittle, transgranular fracture mechanism dominates. Figure 42 shows an area where both ductile and brittle features are observed.

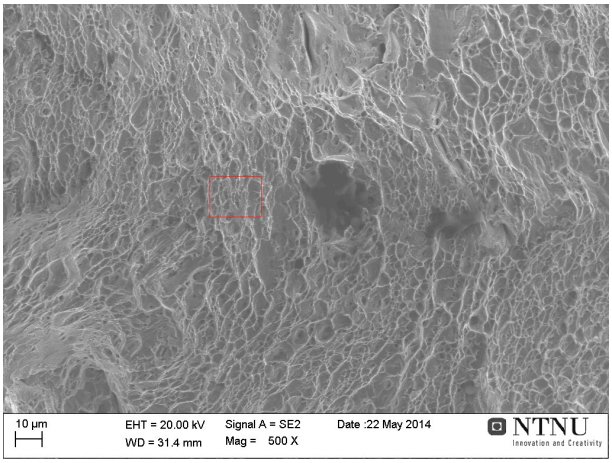

Figure 38: I picture of the "centre" square in Figure 37 at 500X magnification.

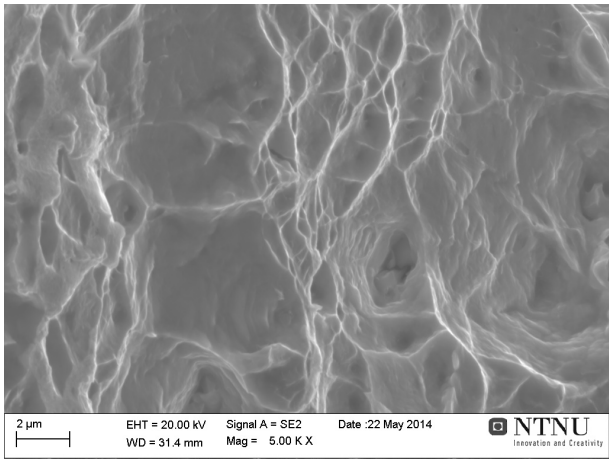

Figure 39: A closer look at the red square in Figure 38.

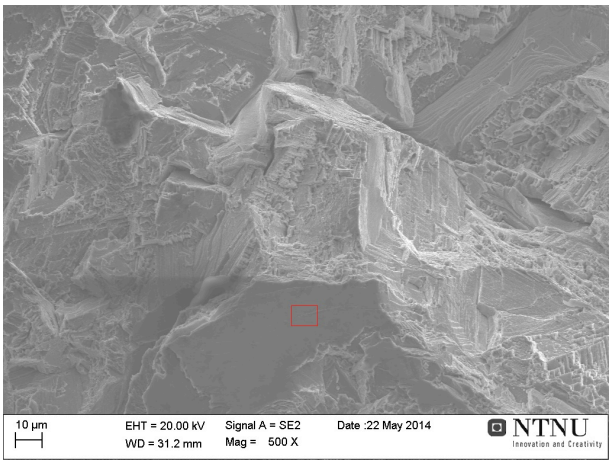

Figure 40: A picture of the red square called "edge" in Figure 37 at 500X magnification.

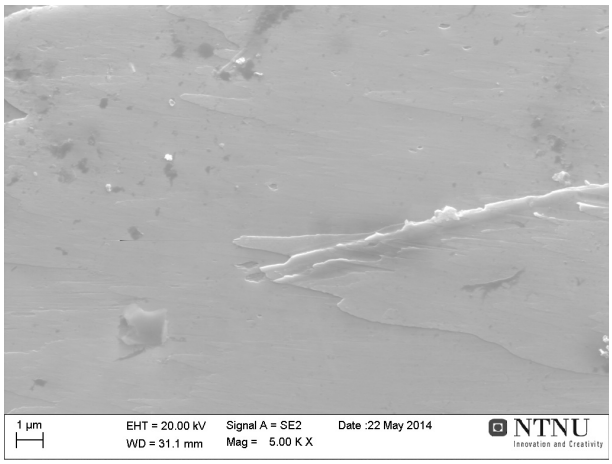

Figure 41: A closer look at the red square in Figure 40.

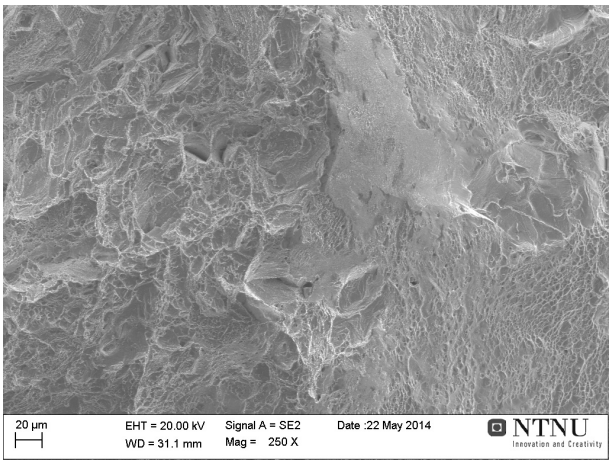

Figure 42: A picture of the fracture surface that shows a mixture of brittle and ductile feature. It is taken in the red square called "mixed" in Figure 37.

4.6.3. Secondary cracks

The side of each standard tensile specimen and HISC specimen were also examined after fracture. The secondary cracks found on the standard tensile specimen are shown in Figure 43 to Figure 46. High magnification was needed to observe the few cracks found on the specimen.

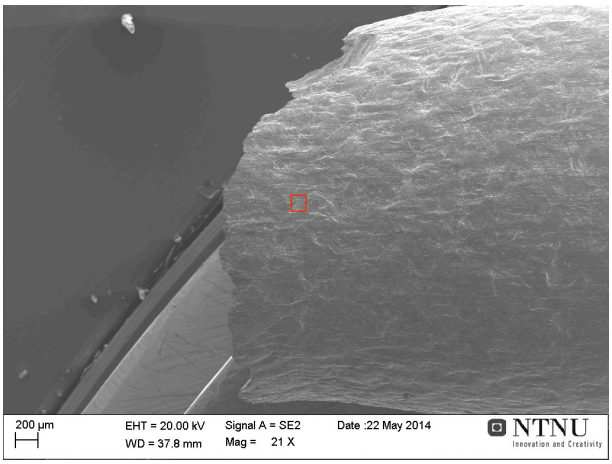

Figure 43: Shows the side of one of the standard tensile test specimen of Alloy 718. Few secondary cracks are observed at this magnification.

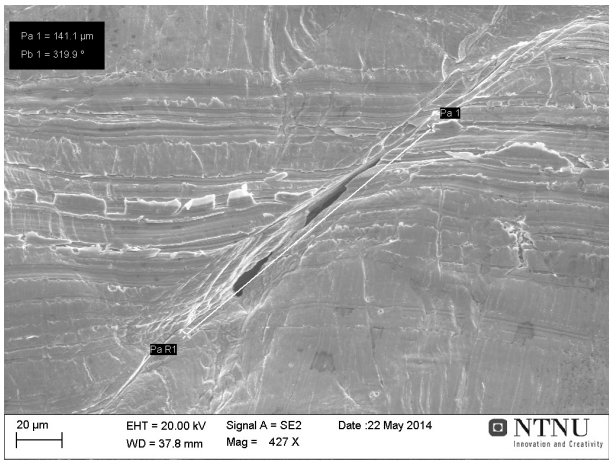

Figure 44: This picture shows the red box in Figure 43 at higher magnification. The crack is measured to 141 µm

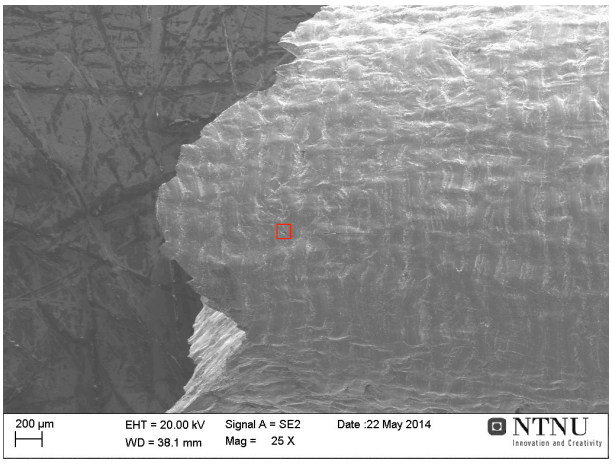

Figure 45: Shows the side of one of the standard tensile test specimen of Alloy 725. Few secondary cracks are observed at this magnification.

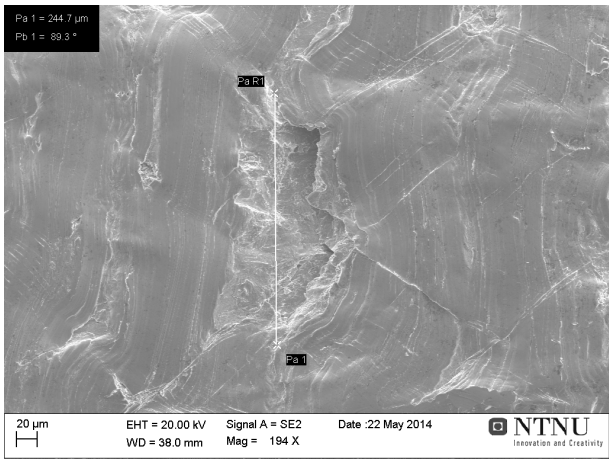

Figure 46: This picture shows the red box in Figure 45 at higher magnification. The crack is measured to 244 µm

Pictures of the secondary cracks found on the HISC samples are presented in Figure 47 and Figure 48. These specimens showed a very different surface. Several large secondary cracks, could be found. Secondary cracks could be observed all over the

reduced area section of the sample. The size of the cracks was smaller further away from the fracture.

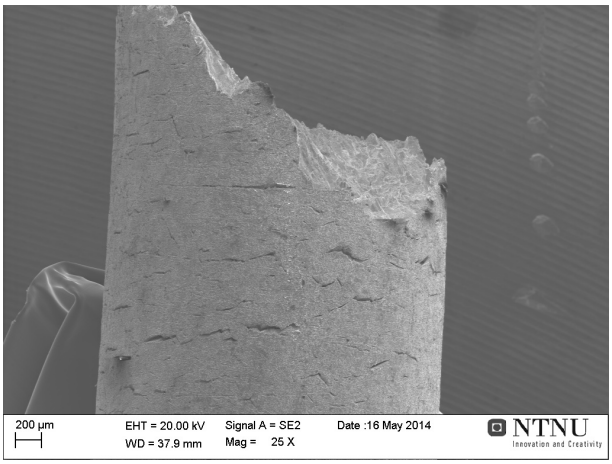

Figure 47: Shows a picture of the secondary cracks found on the surface of a Alloy 718 HISC sample.

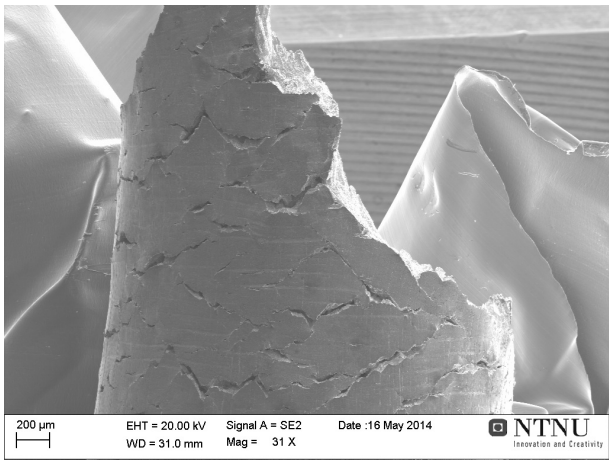

Figure 48: Shows a picture of the secondary cracks found on the surface of a Alloy 725 HISC sample.

4.7. Hydrogen measurements

The results obtained from the hydrogen measurements are presented in Figure 49. The hydrogen was calculated to an accuracy of 0,001 ppm.

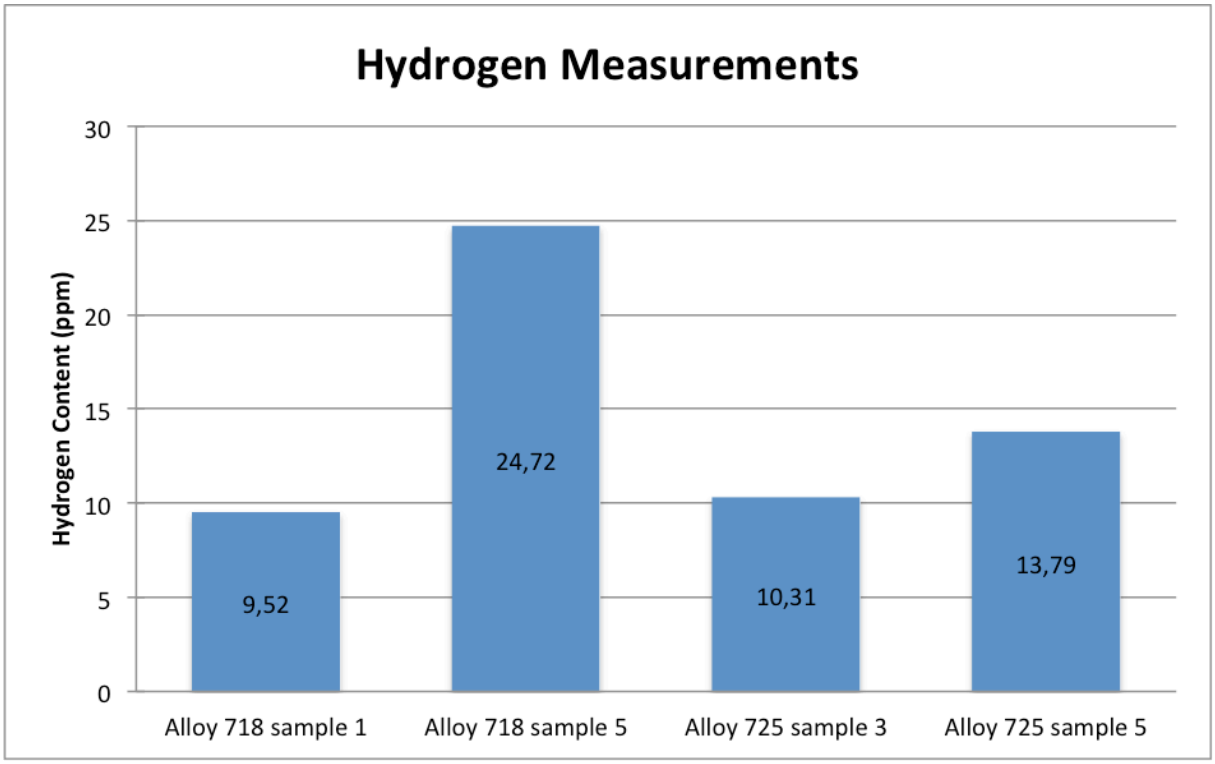

Figure 49: Shows the results from the hydrogen measurements. The x-axis shows which samples has been tested.

4.8. Area measurements

The reduction of area was calculated from the measured diameter of the bars before loading, and the measured diameter of the fracture surfaces. The results are given in Table 10 and Table 11, while they are plotted in Figure 50.

Table 10: Shows the reduction of area and the standard deviations of the reduction of area for Alloy 718. The reduction in reduction of area is calculated for the charged samples.

Alloy 718			
	Reduction of area (%)	STD dev	RRA (%)
Uncharged	46,97	0,745	-
Charged	10,29	3,03	78,1

Table 11: Shows the reduction of area and the standard deviations of the reduction of area for Alloy 725. The Reduction in reduction of area is calculated for the charged samples.

Inconel 725			
	Reduction of area (%)	STD dev	RRA (%)
Uncharged	46,75	0,45	-
Charged	11,86	3,48	74,6

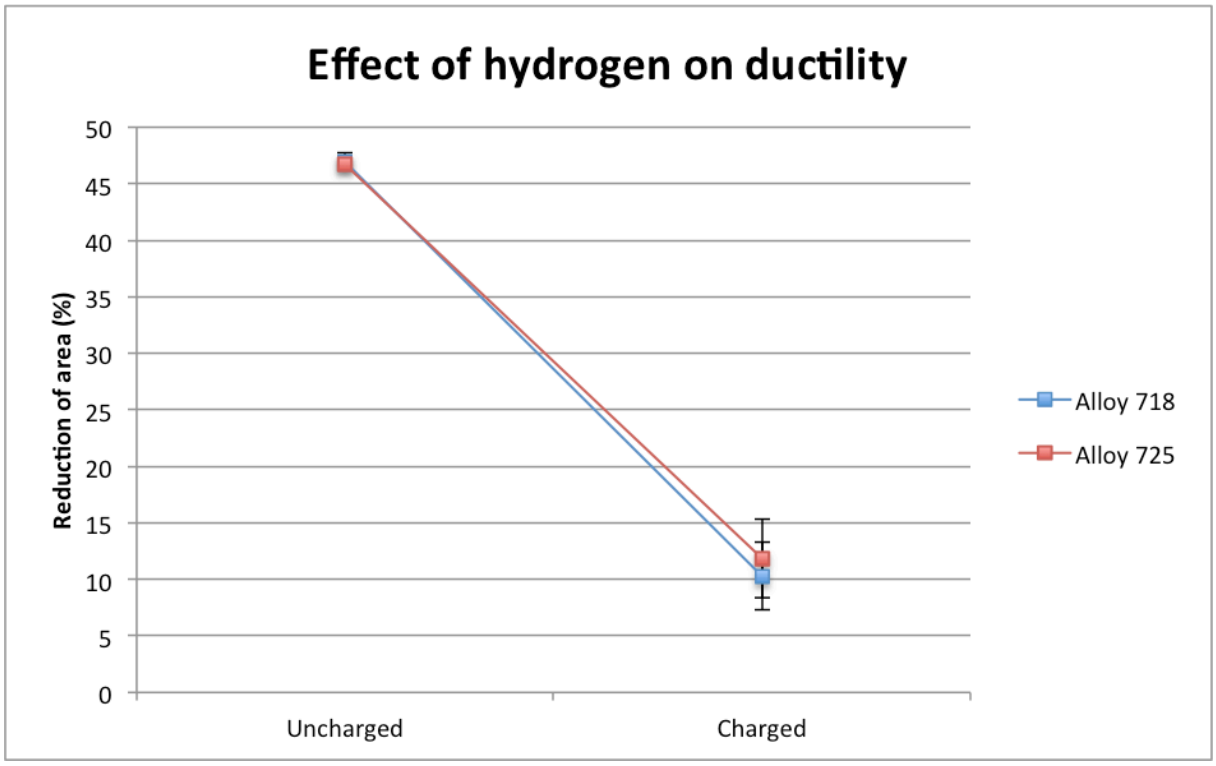

Figure 50: The graph illustrates how the ductility of the two alloys are affected by hydrogen.

5. Discussion

5.1. Pre-charging method

5.1.1. Diffusion calculations

In previous work related to this master thesis, a different pre-charging setup was used. Samples were pre-charged for ten days in 3.5% NaCl solution at 80°C and polarized to -1050 $mV_{Ag/AgCl}$. The following diffusion analysis was used to determine whether to use the old pre-charging setup, or to use a new one where a higher temperature could be used. In addition it illustrates how the hydrogen is distributed over the cross section. Using the diffusion constant given in equation (13.), and a solution of Ficks second law given in equation (14.), one can find the concentration profile of hydrogen in the sample after pre-charging.

$$C(x,t) = C_S - C_S \cdot \operatorname{erf}\left(\frac{x}{2\sqrt{Dt}}\right) \qquad (14.)$$

Here, C_s is the surface concentration, x is the depth and t is the time. Assuming that the limiting factor is the absorption and diffusion of hydrogen, not the evolution, one can set C_s to 1 and compare the concentration profiles obtained. The validity of this assumption is discussed in the next paragraph. This diffusion analyses does not consider the effect of hydrogen trapping, edge effects or other interferences. It does therefore estimate the depth of the hydrogen penetration poorly. This analysis is only used for comparing the two different pre-charging procedures. The obtained concentration profiles for the two different pre-charging setups are presented in Figure 51 and Figure 52.

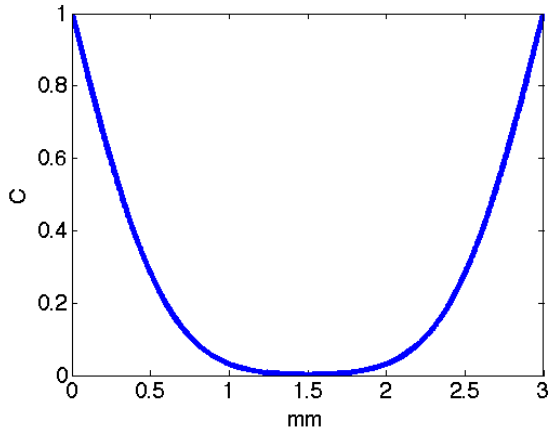

Figure 51: Concentration profile after pre-charging at 120°C for 5 days.

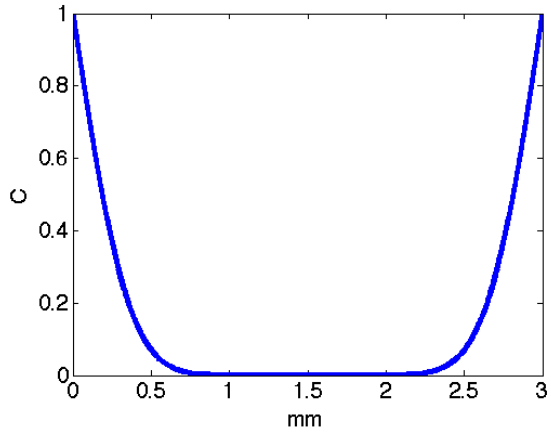

Figure 52: Concentration profile after pre-charging at 80°C for 10 days.

When comparing the two concentration profiles, we can safely say that pre-charging at 120°C is more effective than at 80°C, and that the samples will contain more hydrogen after the pre-charging at 120°C for 5 days.

The assumption that makes it possible to set the C_s equal for both pre-charge setups is not correct. The surface concentration of hydrogen is dependent on the hydrogen evolution, which again is dependent on the temperature and pH of the electrolyte. A lower pH and a higher temperature will increase the hydrogen evolution. This is the case for the new pre-charging method. The C_s will therefore be higher for the new pre-charging setup. This should increase the hydrogen concentration in the samples even more.

Another motivation for using a new pre-charging setup was to avoid a black residue that formed on the sample surfaces during the old pre-charge. This problem was not successfully solved because the new electrolyte decomposed and turned black after one or two days. The electrolyte was changed every second day, and made the pre-charging setup inconvenient. Another practical problem with the new setup was to find a potentiostat that could deliver enough current to polarize the samples. As a result of this current limit, only two samples could be pre-charged at a time. Maybe the biggest problem with the new setup was to maintain contact between the reference electrode and the container where the working and counter electrode was located. Hydrogen bubbles from the working electrode reaction could enter the reference electrode tube and break the connection. The potentiostat would then try to increase the current in both directions and eventually ruin the samples.

5.1.2. Evaluation of the pre-charging method

As seen in Figure 21, Figure 22 and Figure 53 to Figure 60 the current fluctuated severely during the pre-charge. In addition, the average current varied for each pre-charge (see Table 5). Since the hydrogen evolution on the samples is directly related to the net current, the hydrogen evolution will fluctuate as much as the current. It was assumed that this temperature, electrolyte and potential gave a high enough hydrogen evolution rate to make the hydrogen absorption and diffusion the limiting factors. In this way the fluctuations in current should not affect the hydrogen concentrations in the samples. This was however contradicted by the hydrogen measurements (see Figure

49). Samples of the same alloy showed large deviation in the hydrogen content. This is further discussed in chapter 5.5.

To summarize, due to the high temperature the new pre-charge setup should force more hydrogen into the material in less time. There are however flaws to it. Only two samples could be pre-charged at a time. In this way, only two and two samples experienced the same pre-charge, resulting in a large variance in the hydrogen concentration. This combined with the practical problems, makes it an unsuitable pre-charging method. For future work the pre-charging in 3,5% NaCl solution at 80°C should be sufficient for materials with higher diffusivity. A modified version of the new pre-charging setup should be used for materials with a lower diffusivity. Instead of using constant potential, a constant current system should be used. In this way the hydrogen evolution would be the same on all samples, and it would be easy to reproduce the results obtained. An alternative would be to develop a method where all the samples could be pre-charged together.

5.2. Material properties

The tensile properties and grain size found for Alloy 718 matches the values given in the datasheet. This indicates that the microstructure of the material is as desired. The same values for Alloy 725 are, on the other hand, far from the values specified in the datasheet. The yield strength is about 100 MPa below the desired yield strength. A careful microstructural examination could reveal if this lack of strength was due to low amounts of precipitates, large grains or other microstructural effects. The only thing examined in this case was the grain size, which was coarser (ASTM 3.0) than given in the material datasheet (ASTM 3.5-4.5). It is questionable that this alone is enough to reduce the YS by 100 MPa. The Alloy 725 material examined in this work may therefore have a different amount of precipitates and other microstructural effects, than the standard Alloy 725. In this way it may respond differently to hydrogen compared to a material that met the specifications.

As mentioned in the experimental chapter, both alloys were received as forged components. The Alloy 725 samples were extracted from a forged ring while the Alloy 718 samples were extracted from a forged bolt. This forging process may be the reason

for the deviation in the Alloy 725 material properties. If this is the fact, the HISC results obtained in this thesis is applicable for all the Alloy 725 rings manufactured in this way.

5.3. HISC testing

5.3.1. Sources of error

Before evaluating the result from the HISC testing, the uncertainties related to the testing should be discussed. The ring deflection used to control the load in the Cortest proof rings and the diameter of each tensile/HISC specimen was measured with a calliper with an accuracy of 0,02 mm. This uncertainty will be the same for every measurement preformed, and is the limit of how accurate each diameter can be measured. In addition some inaccuracy will occur if the operator use different load on the calliper during each measurement. Using the same operator every day minimized this inaccuracy.

5.3.2. Comparing the conversion charts and the load cell

As mentioned, after the HISC testing was finished, a load cell was used to confirm the values found by using the conversion charts. The values from the conversion charts showed a lower value than the ones obtained by the load cell. This was also discovered in the work done by K. Andersen[6], who used the same Cortest rings and load cell. The Cortest proof rings used here was obtained and calibrated over 20 years ago. It is fair to assume that 20 years of use has altered the ring constants used in the conversion charts. The load cell is relatively new and should be more accurate than the conversion charts. The results from the load cell will therefore be used in the next chapters.

5.3.3. Evaluating HISC results

As expected both alloy are affected by hydrogen. The strength and ductility of both alloys are reduced, although the ductility is more affected than the fracture strength (as shown in Table 12).

Table 12: A summary of how hydrogen affects the mechanical properties of the two alloys.

Material	RRA (%)	Reduction in stress at fracture/YS (%)
Alloy 718	78,08 (±6,13)	6,86 (±4,08)
Alloy 725	74,62 (±6,90)	6,48 (±1,61)

When looking at the values in Table 12, it is hard to differ between the two alloys. The difference in both reduction in RA and reduction in the fracture stress (relative to YS) between the two alloys is to small compared to the standard deviation to differ between them.

One important thing to notice is that Alloy 725 withstands a higher stress (relative to YS) than Alloy 718 during cathodic polarization. From the constant load testing it was found that a safe load for Alloy 725 and Alloy 718 was 123,8 % and 120,4% of YS, respectively. This seems to favour Alloy 725, but one have to bear in mind that the YS of Alloy 718 was about 100 MPa higher than the YS of Alloy 725. Would 123,8 % of YS still be a safe load if the YS of Alloy 725 met the specifications given in the material data sheet? If this were the case, Alloy 725 would in fact be more resistant to hydrogen embrittlement, and endure a higher load during cathodic protection than Alloy 718. It is not possible to answer this question based on the results obtained in this work. Increasing the YS of Alloy 725 to its specifications would alter the microstructure, affecting the susceptibility to hydrogen. It is therefore fair to assume a material that met the YS specifications of Alloy 725 would be affected in a different extent than the material used for this work.

5.4. Fracture surfaces.

Pictures of the fracture surfaces were included in the result. As expected, fracture surface examination of the standard tensile test of both alloys (Figure 29 and Figure 36) revealed dimpled features all over the surface. Combined with the observation of necking, large reduction of area and cup-and-cone similar surfaces, this implies completely ductile fracture. This was not the case for the HISC fracture surfaces. Here, faceted and flat features existed close to the surface. This can be observed in Figure 30 and Figure 37. These features could also be observed near the centre of the fracture surface, although to a lesser extend. The centre of the fracture surfaces were covered of dimples (Figure 31 and Figure 38). Neither necking nor the cup-and-cone feature could be seen on the HISC samples. All these observations indicate a reduction of ductility due to the hydrogen. These observations were made on the HISC samples of both alloys.

Similar work on this subject has revealed a brittle outer ring on the fracture surfaces when hydrogen was introduced to the material[26]. An idea for this work was to try to estimate the depth of this ring and try to relate it to the HE susceptibility. Using this depth and together with some diffusional analysis could give interesting results regarding a critical hydrogen content for HISC to occur. Due to no clear transition from brittle to ductile features, it was not possible to determine the depth of this ring.

Another observation that was made in the SEM was the presence of secondary cracks all over the sides of the HISC samples (see Figure 47 and Figure 48). This was in great contrast to the standard tensile test specimen, which showed few and small cracks near the fracture surface (see Figure 43 and Figure 45). This difference may occur because the hydrogen concentration in the surface of the sample makes the outer layer very brittle. This layer will crack, causing several cracks over the surface. One of these cracks will propagate and cause final fracture of the sample.

5.5. Hydrogen content

The hydrogen content was measured in two samples of each alloy. This was done externally by SINTEF – Materials and Chemistry. The results are presented in Figure 49. One weakness with these measurements is that it only gives the total hydrogen in a small volume (about 0,5 grams) and does not say anything about the concentration profile through the sample. It should therefore be kept in mind that the concentration will be lower in the centre and higher at the edge of the sample cross section.

The hydrogen measurements showed a larger deviation in the hydrogen concentration than expected. Sample 1 and sample 5 of the Alloy 718 should have about the same hydrogen concentration. However, the hydrogen concentration deviates severely (see Table 13). This was not as expected and implies, as previously discussed, that the pre-charging procedure is not precise enough.

The result from the hydrogen measurement did shed some light on why the stress values at fracture and RA varied as much as it did. As shown in Table 13, the samples showing the highest stress at fracture and RA is also the ones with the lowest H-concentration. As expected, more hydrogen in the samples gives a lower stress at

fracture and a lower RA. The same consistency does not exist for the average current during pre-charging and the hydrogen content. It was expected that a higher current should give a higher hydrogen concentration. This is true for the Alloy 718 samples, but not the Alloy 725 samples. This indicates that the current during pre-charging may not be the most important factor for hydrogen uptake.

Table 13: A table comparing the hydrogen content of the different samples with their stress level at fracture (relative to YS), RA and Average current during pre-charge.

Sample	Hydrogen content (wppm)	Fracture (relative to YS)	RA	Average current during pre-charging
Alloy 718 sample 1	9,52	137,22	13,9	0,395
Alloy 718 sample 5	24,72	126,18	9,94	0,642
Alloy 725 sample 3	10,31	140,49	16,2	0,485
Alloy 725 sample 5	13,79	135,94	9,00	0,484

Using the values given in Table 13 one can speculate in the hydrogen concentrations in the rest of the samples. Comparing the stress at fracture value for those samples tested for hydrogen with those not tested, should give an indication. From Table 7 one can see that Alloy 718 sample 8, 10, 2 and 5 have similar stress at fracture values. It is therefore fair to assume that sample 8, 10 and 2 have about the same hydrogen concentration as sample 5. The hydrogen concentration in sample 5 were measured to 24,72 wppm.

In the same way one can estimate the hydrogen concentration in the rest of the Alloy 725 samples. Table 8 shows that sample 3 represent the highest stress at fracture while sample 5 represent one of the lowest. It is therefore fair to assume that the Alloy 725 samples have a hydrogen concentration between 10 and 14 wppm. The hydrogen concentration of Alloy 718 sample 5 and Alloy 725 sample 3 is therefore used further in the discussion.

One can consider this result in different ways. The hydrogen uptake in the Alloy 718 samples were about double that of the Alloy 725 samples. In other words, it took less

time to obtain higher hydrogen concentrations in the Alloy 718. This would indicate that Alloy 718 is more susceptible to HISC. On the other hand, it seems that the ductility of the Alloy 725 samples are reduced by the same amount as the Alloy 718 samples, even though the hydrogen concentration is lower in the Alloy 725 samples. This would indicate the opposite.

It is clear that the hydrogen concentrations were not as consistent as expected, but it is still possible to draw conclusions based on the obtained data.

Comparing the obtained hydrogen concentration values to those obtained by others, could give an indication of how effective the pre-charging procedure is. L. Liu et al. charged Alloy 718 samples in a molten salt bath at 200°C for 30 hours. They got a uniform concentration of 20 wppm through the specimen [39]. P. D. Hicks and C. J. Altstetter used a molten salt bath to charge Alloy 718 samples at 250 °C and obtained uniform hydrogen concentration of 49 wppm [50]. It is very interesting that a uniform concentration profile was obtained with these pre-charging setups. The procedure for pre-charging in these two articles show how one can obtained a uniform hydrogen concentration through a thin sample, and could be interesting to try in further work.

5.6. Comparing the result with previous work

K. Andersen[6] used the same setup for testing the HISC susceptibility of super duplex stainless steel (SDSS). The only difference was, that he used the 3.5% NaCl pre-charging setup, as previously described. SDSS is a family of alloys that consists of a 50/50 mix of two phases, namely austenite (FCC structure) and ferrite (BCC structure). Since both SDSS and the alloys examined in this thesis are used subsea, it is interesting to compare the susceptibility of the alloys. Results from this work (Alloy 718 and Alloy 725) are compared with results from K. Andersens work in Table 14.

The reduction in ductility was measured in two different ways. K. Andersen calculated this by converting stress values to strain values by using the stress-strain graph for the material. In this way he could express the ductility as reduction in strain. He got very high standard deviations in the strain values. These values should therefore be used carefully. It is possible to relate the strain, and therefore the reduced elongation to RA

and RRA, as is used in this work. However, since the strain values from K. Andersens work is interpolated from stress values, and not directly measured, comparing the ductility values from his experiments and those obtained in this work would not be correct. The last recorded stress at no fracture seems however to be reduced more for the SDSS materials.

Table 14: A table comparing values obtained in this work, with the work of K. Andersen [6].

Material	Crystal structure	Grain size/Austenite spacing* (µm)	Measured Hydrogen (wppm)	Reduction in ductility (%)	UTS/YS (%)	Last recorded "No fracture" value (% of YS)	Reduction in stress at fracture
SDSS HIP	BCC/FCC	12,9	132,8	35 **	133	112,6	7,52
SDSS Forged	BCC/FCC	51,5	291	41 **	132	104,8	11,36
Alloy 718	FCC	85	24,72	78,09	136,5	121,29 ***	6,86
Alloy 725	FCC	108,5	13,79	74,62	147,2	133,07	6,48

*** Since SDSS is a duplex material (consists of austenite and ferrite) and the size and shape of the different phases can be different, the austenite spacing (distance between austenite grains) is a more correct term than grain size.**
****These ductility measurements were calculated by transforming stress values to strain, not RA.**
***** This value is the average of sample 2, 5, 8 and 10.**

As mentioned in the theory, there is a clear difference in the hydrogen diffusivity and solubility in FCC and BCC metals. FCC has a slow diffusivity and high solubility of hydrogen, while BCC metals has a high diffusivity and a low solubility. This is probably the reason for the major difference in the hydrogen concentration of the FCC alloys (718 and 725) and the SDSS. Due to the ferrite grains in SDSS, the hydrogen diffusivity will be greatly enhanced and the metal will reach saturation faster. However, it is very surprising that K. Andersen obtained a much higher concentration in SDSS than P. D. Hicks and C. J. Altstetter did in Alloy 718[50]. The solubility should be higher in Alloy 718 and the samples used by P. D. Hicks and C. J. Altstetter were completely saturated.

Considering that the SDSS materials had a much higher hydrogen concentration and responded less to it (lower loss of ductility and almost the same loss in strength), it is

fair to propose that SDSS is more resistant to HISC than Alloy 725 and Alloy 718. However, one advantage with Alloy 725 and Alloy 718 is the reduced hydrogen diffusivity, which may increase the time before HISC occurs (compared to SDSS).

5.7. Further work

The most important improvement to the test procedure used in this project would be to get a more reliable pre-charge. To be able to make strong conclusions, the pre-charging of the samples should be as similar as possible. The use of constant current density during pre-charging should be considered. A setup where all samples can be pre-charged at once should be used. In this way all samples will experience the same conditions during pre-charging and results with high reproducibility would be obtained.

As experienced in this project, when comparing two alloys of similar strength, they should have gone through the same manufacturing steps. Alloy 718 was received as a forged bolt, while Alloy 725 was received as a forged ring. This gave a deviation in the YS of Alloy 725 compared to the specifications. If the alloy had YS as specified, it might have responded differently to the hydrogen. Alloy 725 material with YS as specified should therefore be tested.

For further work on these alloys, it would be very interesting to investigate how different microstructural features affect the HISC susceptibility. As mentioned in the theory, it is well established how the different phases and precipitates in these alloys affects the hydrogen embrittlement susceptibility. The grain size effect is however not well established, and is a natural next step for this work.

6. Conclusion

Tensile bars of Alloy 718 and Alloy 725 were stepwise loaded in Cortest proof rings to investigate the HISC susceptibility of the alloys. The fracture surfaces were examined and the hydrogen concentration measured. These results were used to compare the performance of both alloys. The following concluding remarks were drawn from the results obtained in this work:

- Both alloys are severely affected by hydrogen. It was shown that a higher hydrogen concentration gave a greater loss of ductility and strength. The effect of hydrogen could also be observed on the fracture surfaces, where a transition from ductile to brittle features where observed.
- Hydrogen gave a reduction in both strength and ductility of the alloys. The RRA due to hydrogen for Alloy 718 and Alloy 725 was 78,08 (±6,13) % and 74,62 (±6,90) %, respectively.
- The average stress at fracture was reduced by 6,86 (±4,08) % and 6,48 (±1,61) % for Alloy 718 and Alloy 725, respectively.
- The constant load tests revealed a higher safe stress (relative to YS) for Alloy 725 (123,8 %) compared to Alloy 718 (120,4 %). This indicates a lower HISC susceptibility for Alloy 725.

7. References

1. Standard, N., *Petroleums- og naturgassindustri: Materialer for bruk i H2S-miljøer i olje- og gassproduksjon., Del 3, Sprekkmotstandsdyktige CRA (korrosjonsmotstandige legeringer) og andre legeringer (ISO 15156-3:2009)*. 2009, Oslo: Standard Norge. 73 s.
2. McCoy, S., et al., *High performance age-hardenable nickel alloys solve problems in sour oil and gas service.* Balance, 2002. **14**: p. 16.5.
3. Shademan, S.S., J.W. Martin, and A.P. Davis, *Uns N07725 Nickel Alloy Connection Failure*. NACE International.
4. T. Cassagne, M.B., D. Hills, C. Duret, *Understanding field failures of alloy 718 forging materials in HP/HT wells* in *European corrosion congress; EUROCORR 2008. Managing corrosion for sustainability*, E.F.o. Corrosion, Editor. 2008. p. 12.
5. Huizinga, S., et al., *Offshore Nickel Alloy Tubing Hanger and Duplex Stainless Steel Piping Failure Investigations.* CORROSION 2003, 2003.
6. Andersen, K., *HISC in Super Duplex Stainless Steels : A study of the relation between microstructure and susceptibility to hydrogen induced stress cracking*. 2013: Institutt for materialteknologi\. 114\.
7. Dieter, G.E., *Mechanical Metallurgy SI metric edition*. 1988: MxGraw-Hill Book Co. 739.
8. Askeland, D.R. and P.P. Phulé, *Science & Engineering of Materials*. 2006: Cengage Learning.
9. Anderson, T.L., *Fracture mechanics: Fundamentals and Applications*. 3 ed. 2005: CRC press.
10. Gangloff, R., *Comprehensive Structural Integrity, vol. 6, I. Milne, RO Ritchie, and B. Ksrihalco, Eds*. 2003, New York, NY), Elsevier Science.
11. Page, R.A. and W.W. Gerberich, *The effect of hydrogen source on crack initiation in 4340 steel.* Metallurgical Transactions A, 1982. **13**(2): p. 305-311.
12. Stroe, M.E., *Hydrogen embrittlement of ferrous materials.* Romania: Universite Libre De Bruxelles, 2006.
13. Yao, Y., X. Pang, and K. Gao, *Investigation on hydrogen induced cracking behaviors of Ni-base alloy.* International Journal of Hydrogen Energy, 2011. **36**(9): p. 5729-5738.
14. Pound, B.G., *Hydrogen trapping in precipitation-hardened alloys.* Acta Metallurgica et Materialia, 1990. **38**(12): p. 2373-2381.
15. Kimura, A. and H.K. Birnbaum, *Hydrogen induced grain boundary fracture in high purity nickel and its alloys—Enhanced hydrogen diffusion along grain boundaries.* Acta Metallurgica, 1988. **36**(3): p. 757-766.
16. Oudriss, A., et al., *The diffusion and trapping of hydrogen along the grain boundaries in polycrystalline nickel.* Scripta Materialia, 2012. **66**(1): p. 37-40.
17. Harris, T.M. and M. Latanision, *Grain boundary diffusion of hydrogen in nickel.* Metallurgical Transactions A, 1991. **22**(2): p. 351-355.
18. Yao, J. and J.R. Cahoon, *Experimental studies of grain boundary diffusion of hydrogen in metals.* Acta Metallurgica et Materialia, 1991. **39**(1): p. 119-126.
19. Lynch, S., *Metallographic contributions to understanding mechanisms of environmentally assisted cracking.* Metallography, 1989. **23**(2): p. 147-171.

20. Birnbaum, H.K. and P. Sofronis, *Hydrogen-enhanced localized plasticity—a mechanism for hydrogen-related fracture.* Materials Science and Engineering: A, 1994. **176**(1–2): p. 191-202.
21. Birnbaum, H.K., *Mechanisms of hydrogen related fracture of metals*. 1989, DTIC Document.
22. Lynch, S.P., *A fractographic study of hydrogen-assisted cracking and liquid-metal embrittlement in nickel.* Journal of Materials Science, 1986. **21**(2): p. 692-704.
23. Robertson, I. and H. Birnbaum, *An HVEM study of hydrogen effects on the deformation and fracture of nickel.* Acta Metallurgica, 1986. **34**(3): p. 353-366.
24. Oriani, R. and P. Josephic, *Testing of the decohesion theory of hydrogen-induced crack propagation.* Scripta Metallurgica, 1972. **6**(8): p. 681-688.
25. Robertson, I.M., H.K. Birnbaum, and P. Sofronis, *Chapter 91 Hydrogen Effects on Plasticity*, in *Dislocations in Solids*, J.P. Hirth and L. Kubin, Editors. 2009, Elsevier. p. 249-293.
26. Fournier, L., D. Delafosse, and T. Magnin, *Cathodic hydrogen embrittlement in alloy 718.* Materials Science and Engineering: A, 1999. **269**(1): p. 111-119.
27. Lee, H.-T. and W.-H. Hou, *Development of fine-grained structure and the mechanical properties of nickel-based Superalloy 718.* Materials Science and Engineering: A, 2012. **555**(0): p. 13-20.
28. Liu, L., et al., *Study of the effect of δ phase on hydrogen embrittlement of Inconel 718 by notch tensile tests.* Corrosion science, 2005. **47**(2): p. 355-367.
29. Slama, C. and M. Abdellaoui, *Structural characterization of the aged Inconel 718.* Journal of alloys and compounds, 2000. **306**(1): p. 277-284.
30. Azadian, S., L.-Y. Wei, and R. Warren, *Delta phase precipitation in Inconel 718.* Materials Characterization, 2004. **53**(1): p. 7-16.
31. Maguire, M. and J. Michael. *Weldability of alloy 718, 625 and Variants*. in *Third International Special Emphasis Symposium on Superalloys*. 1994.
32. Chamanfar, A., et al., *Microstructural characteristics of forged and heat treated Inconel-718 disks.* Materials & Design, 2013. **52**(0): p. 791-800.
33. Bhavsar, R.B., A. Collins, and S. Silverman, *Use of alloy 718 and 725 in oil and gas industry.* Minerals, Metals and Materials Society/AIME, Superalloys 718, 625, 706 and Various Derivatives(USA), 2001: p. 47-55.
34. Cieslak, M., et al., *The solidification metallurgy of alloy 718 and other Nb-containing superalloys.* Superalloy, 1989. **718**: p. 59-68.
35. E. L Hibner, S.K.M., H.W. Sizek, *Elevated temperature tensile and creep rupture properties of INCONEL Alloy 725.* Superalloys 718, 625, 706 and various derivatives, 1997: p. 491-501.
36. Norge, S., *Petroleums- og naturgassindustri - Materialer for bruk i H2S-miljøer i olje- og gassproduksjon - Del 3: Sprekkmotstandsdyktige CRA (korrosjonsmotstandige legeringer) og andre legeringer (ISO 15156-3:2009)*. 2010, Standard Norge. p. 84.
37. Sjoberg, G., et al., *Grain boundary 6-phase morphologies, carbides and notch rupture sensitivity of cast alloy 718.* Superalloys 718, 612 and Various Derivatives.
38. G. Sjoberg, D.C. *Hydrogen Embrittlement of Cast Alloy 718 Effects of Homogenization, Grain Size and δ-Phase*. in *Superalloys 718, 625, 706 and Various Derivatives (2001)*. 2001.
39. Liu, L., et al., *Effects of precipitation phases on the hydrogen embrittlement sensitivity of Inconel 718.* Science and Technology of Advanced Materials, 2002. **3**(4): p. 335-344.

40. Pound, B., *The effect of aging on hydrogen trapping in precipitation-hardened alloys.* Corrosion science, 2000. **42**(11): p. 1941-1956.
41. Lillard, J., R. Kelly, and R. Gangloff, *Effect of Electrode Potential on Stress Corrosion Cracking and Crack Chemistry of a Nickel-Base Superalloy.* Corrosion97, 1997.
42. Hibner, E.L. and L.E. Shoemaker, *High Strength, Corrosion-Resistant Superalloy Fasteners, Springs, and Hardware for Marine Service.*
43. Robertson, W.M., *Hydrogen permeation and diffusion in inconel 718 and incoloy 903.* Metallurgical Transactions A, 1977. **8**(11): p. 1709-1712.
44. Jebaraj, J.J., D.J. Morrison, and I.I. Suni, *Hydrogen diffusion coefficients through Inconel 718 in different metallurgical conditions.* Corrosion Science, 2014. **80**: p. 517-522.
45. Olden, V., C. Thaulow, and R. Johnsen, *Modelling of hydrogen diffusion and hydrogen induced cracking in supermartensitic and duplex stainless steels.* Materials & design, 2008. **29**(10): p. 1934-1948.
46. Norge, S., *Metallic materials - Tensile testing - Part 1: Method of test at room temperature (ISO 6892-1:2009)*. 2009. p. 76.
47. international, A., *ASTM E407-07 Standard Practice for Microetching Metals and Alloys.* 2014.
48. international, A., *ASTM E112- 12 Standard Test Methods for Determining Average Grain Size*. 2013.
49. TM, N., *Laboratory testing of metals for resistance to sulfide stress cracking and stress corrosion cracking in H2S environments.* Houston, TX: NACE, 2005.
50. Hicks, P.D. and C.J. Altstetter, *Internal hydrogen effects on tensile properties of iron- and nickel-base superalloys.* Metallurgical Transactions A, 1990. **21**(1): p. 365-372.

Appendix A

Figure 53 to Figure 60 show the pre-charging curves for the rest of the samples. All the potentials are here measured against a $Hg/HgSO_4$ reference electrode.

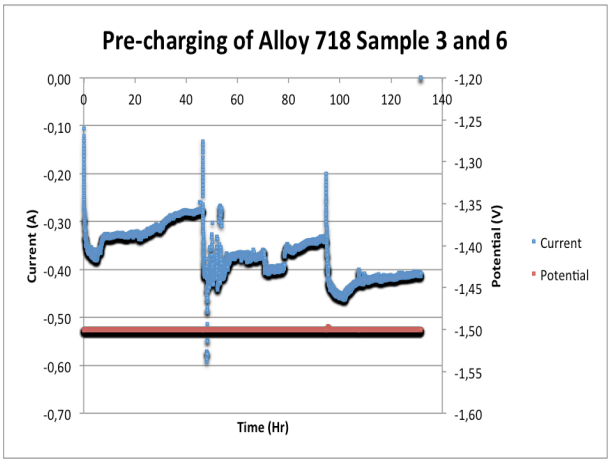

Figure 53 Pre-charging of Alloy 718 sample 3 and 6.

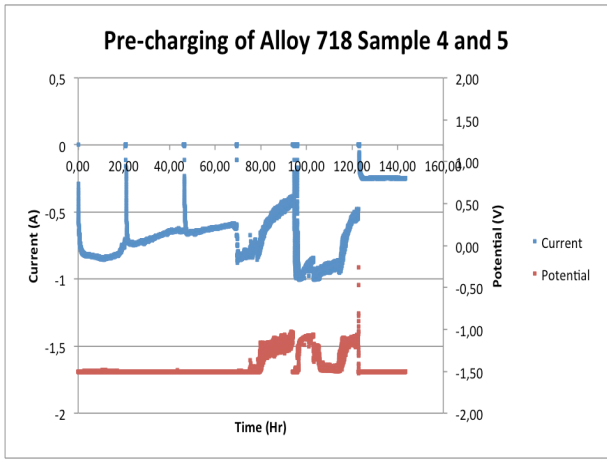

Figure 54 Pre-charging of Alloy 718 sample 4 and 5.

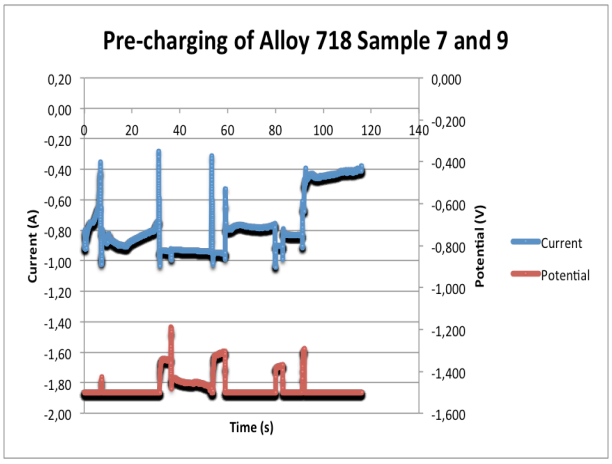

Figure 55 Pre-charging of Alloy 718 sample 7 and 9.

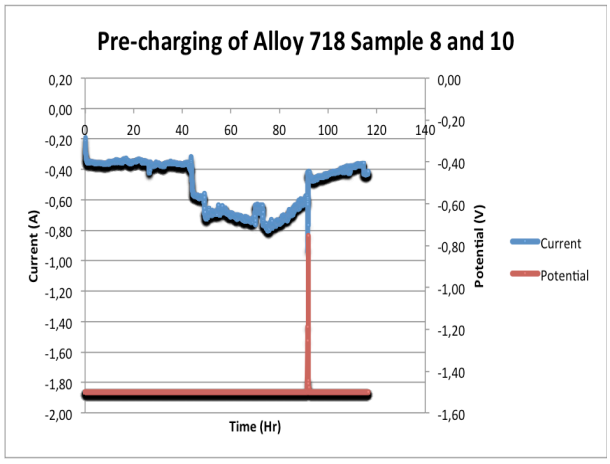

Figure 56 Pre-charging of Alloy 718 sample 8 and 10.

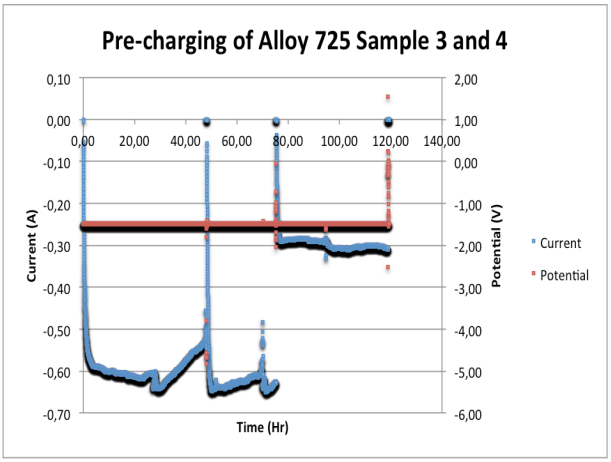

Figure 57 Pre-charging of Alloy 735 sample 3 and 4.

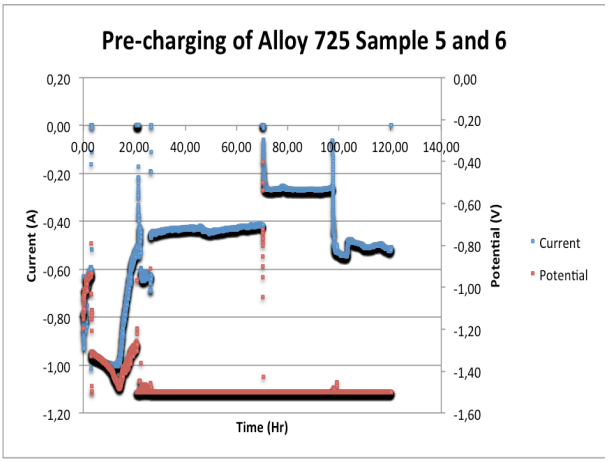

Figure 58 Pre-charging of Alloy 735 sample 5 and 6.

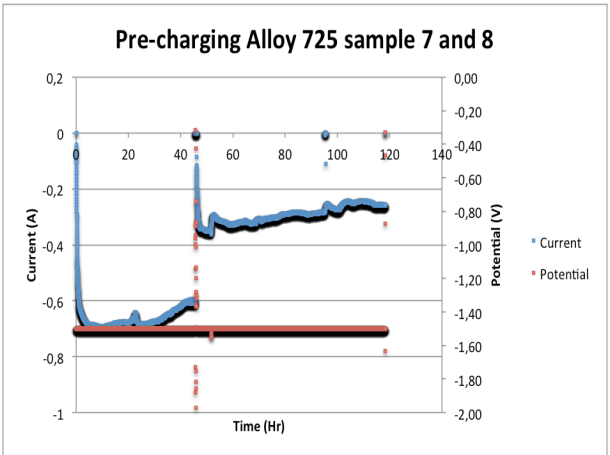

Figure 59 Pre-charging of Alloy 735 sample 7 and 8.

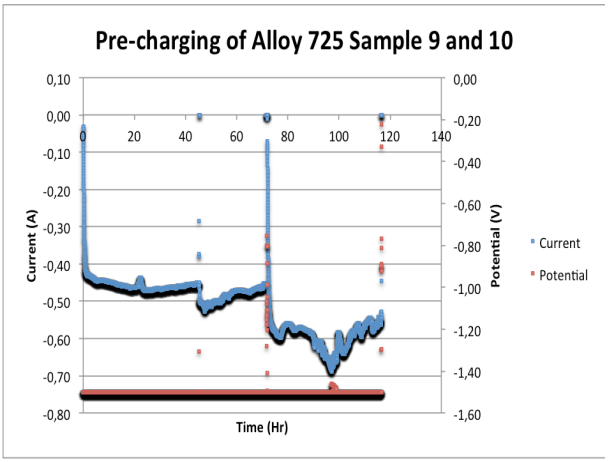

Figure 60 Pre-charging of Alloy 735 sample 9 and 10.